

This is a preprint of the paper. pp. 1–35
This is a preprint of the paper.
This is a preprint of the paper.
This is a preprint of the paper.

A Data Fusion Model for Meteorological Data using the INLA-SPDE method

Stephen Jun Villejo  ^{1,4,*} Sara Martino,² Finn Lindgren³
 and Janine B Illian¹

¹School of Mathematics and Statistics, University of Glasgow, Glasgow, United Kingdom, ²Department of Mathematical Sciences, Norwegian University of Science and Technology, Trondheim, Norway, ³School of Mathematics, College of Science and Engineering, University of Edinburgh, Edinburgh, United Kingdom and ⁴School of Statistics, University of the Philippines Diliman, Quezon City, Philippines

*Corresponding author. stephen.villejo@glasgow.ac.uk

ABSTRACT

This work aims to combine two primary meteorological data sources in the Philippines: data from a sparse network of weather stations and outcomes of a numerical weather prediction model. To this end, we propose a data fusion model which is primarily motivated by the problem of sparsity in the observational data and the use of a numerical prediction model as an additional data source in order to obtain better predictions for the variables of interest. The proposed data fusion model assumes that the different data sources are error-prone realizations of a common latent process. The outcomes from the weather stations follow the classical error model while the outcomes of the numerical weather prediction model involves a constant multiplicative bias parameter and an additive bias which is spatially-structured and time-varying. We use a Bayesian model averaging approach with the integrated nested Laplace approximation (INLA) for doing inference. The proposed data fusion model outperforms the stations-only model and the regression calibration approach, when assessed using leave-group-out cross-validation (LGOCV). We assess the benefits of data fusion and evaluate the accuracy of predictions and parameter estimation through a simulation study. The results show that the proposed data fusion model generally gives better predictions compared to the stations-only approach especially with sparse observational data.

KEYWORDS: data fusion, integrated nested Laplace approximation (INLA), Bayesian model averaging

INTRODUCTION

A common aim in spatial statistical modelling is to predict values of a spatial variable at unsampled locations, based on measurements taken at a finite – and often relatively small – number of locations. In the context of environmental sciences and meteorology in particular, data on e.g. air-quality, environmental pollution, surface temperature, or rainfall are collected through a network of monitoring stations [29, 31, 12, 25, 14, 3, 28, 30]. These data are used for prediction, and for understanding the spatio-temporal dynamics of the underlying processes and the impact of these variables on potential outcomes of interest, such as health outcomes. However, due to the high maintenance costs, the monitoring networks are typically spatially sparse [29]. Increasingly, data from additional sources derived from satellite images or outcomes of numerical models with a high spatial resolution are available. These can be used jointly with the monitoring data to improve the accuracy of predictions in a process that combines information from different data sources and is often referred to as *data fusion* or *data assimilation* [6, 21, 29]. The goal is to exploit the better spatial resolution of the additional data to fill gaps in areas only sparsely covered by the monitoring stations in order to predict and map the variables into space with more accuracy at smaller scales than based on the monitoring stations data alone. However, a general issue that is common in attempts to combine data from more than one source is that the various data streams differ in

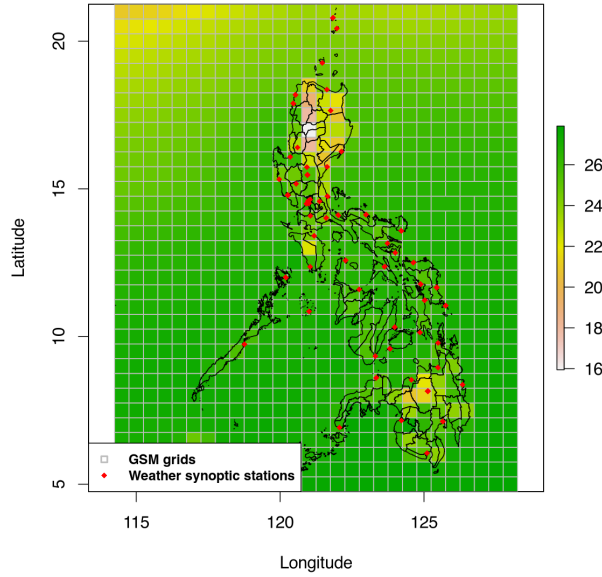


Fig. 1. Meteorological data sources for PH: a sparse network of weather synoptic stations and an outcome of a numerical weather prediction model called Global Spectral Model. The measurements are monthly aggregated values of temperature for August 2019.

their quality. Numerical or satellite data, specifically, are often biased due to calibration issues, and these biases have to be accounted for in the modelling process. Motivated by a data application of meteorological data from the Philippines, we develop a joint modeling methodology that not only flexibly accounts for differences in data quality, but also allows us to gauge the quality of the different data sources.

In particular, this work combines two primary meteorological data sources for the Philippines: observational data from a sparse network of weather synoptic stations, and simulated outcomes from a numerical weather prediction model called the *Global Spectral Model* [39], which provides broad spatial coverage but typically biased due to sensitivity to model initialization and parameterization. The observational data from the weather stations are likely to be less biased, but they provide limited spatial coverage since key areas in space are under-sampled, as is evident in Figure 1. It is therefore potentially advantageous to simultaneously use both data sources through data fusion. Unlike approaches discussed in the literature so far, which are discussed in Section 1.2, this work accounts for calibration biases in the data fusion model, specifies a flexible bias formulation, defines a single and interpretable latent process for the different data sources, and specifies a measurement error for the monitoring stations data. A simulation study compares our proposed data fusion approach to the stations-only model. In the data application, we compare the predictions derived from the proposed data fusion approach, a model based on the data from the stations only, and another approach for data fusion called regression calibration using leave-group-out cross-validation [33, 2]. Although the data application of the proposed data fusion model in this work only considers two data sources, the model and the framework extend to more than two data sources and are relevant beyond this specific scenario.

Meteorological data from the Philippines

The Philippines is an archipelagic country, covering an area of ca. 300 thousand km² (see Figure 1), situated in tropical Southeast Asia. The eastern part and some southern parts of the country are mostly classified as tropical rainforest and is characterized by no distinct wet or dry season and a relatively high rainfall all year round [27]. On the other hand, most of the country's western section is classified as tropical monsoon or tropical Savannah and is characterized by pronounced dry and wet seasons [7]. Such spatio-temporal interaction is the basis for the climate types of the Philippines [39].

The *Philippine Atmospheric, Geophysical and Astronomical Services Administration* (PAGASA) maintains a network of 56 weather synoptic stations which regularly record several meteorological variables such as temperature, relative humidity, and precipitation. The spatial locations of the weather stations are shown

in Figure 1. It is a sparse network relative to the total surface area of the country. Some regions, especially in the northern part, are heavily undersampled. Reconstructing meteorological variable surfaces based only on the weather stations would therefore result in high uncertainty. To augment this sparsity problem in the stations data, PAGASA utilizes the outcomes of the *Global Spectrum Model* (GSM), which is a numerical weather prediction model maintained by the Japanese Meteorological Agency. The GSM provides forecast outputs of up to 132 hours four times a day (with initial times 0000, 0600, 1200, and 1800 UTC) within 4 hours of the initial time, and up to 264 hours twice a day (with initial time 0000 and 1200 UTC) within 7 hours of the initial time. As an example, Figure 1 shows the map of mean temperatures from the GSM for August 2019 at a spatial resolution of 0.5 degree, which corresponds to approximately 55km × 55 km. Although the figure shows the outcomes are gridded, these outcomes are interpreted by PAGASA as point-referenced at the centroids [39].

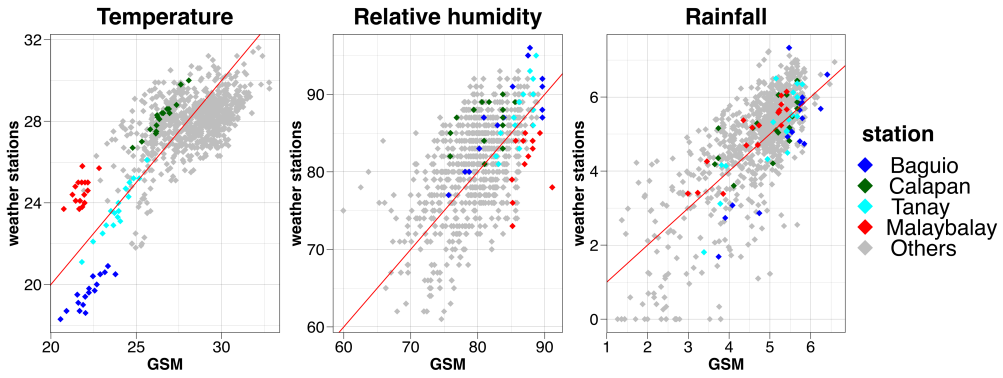


Fig. 2. Scatterplot of the observed values at the weather stations versus interpolated outcomes of the GSM for three meteorological variables: temperature, relative humidity, and log-transformed rainfall. The plot shows the discrepancies in the values between the two data sources.

The GSM outcomes have a much larger spatial coverage, but it is known that outputs from numerical weather models are biased [29, 6]. To assess this, we initially do spatial interpolation using the GSM values on three meteorological variables of interest – temperature, relative humidity, and log-transformed rainfall amounts – and then predict the values at the locations of the weather stations. This is done by fitting the following geostatistical model:

$$w(\mathbf{s}, t) = \beta_0 + \beta_1 z(\mathbf{s}, t) + \xi(\mathbf{s}, t),$$

where $w(\mathbf{s}, t)$ is the observed value of the meteorological variable from the GSM at the spatial grid with centroid \mathbf{s} , $z(\mathbf{s}, t)$ is a known covariate, and $\xi(\mathbf{s}, t)$ is a spatio-temporal random effect. For temperature and relative humidity, we used the elevation variable as covariate. For log-transformed rainfall, we used the relative humidity as the covariate. We assume that $\xi(\mathbf{s}, t)$ evolves in time as an autoregressive process of order 1, i.e.,

$$\xi(\mathbf{s}, t) = \phi \xi(\mathbf{s}, t - 1) + \omega(\mathbf{s}, t),$$

where $|\phi| < 1$ and $\omega(\mathbf{s}, t)$ is a time-independent Gaussian process with a Matérn covariance function specified in Equation (22) and which follows the stationary distribution of the process at time 1. We fit this model using INLA and the SPDE method [41, 32]. We then predict the values of $w(\mathbf{s}, t)$ at the locations of the weather stations and then compare the predicted and the observed values. The resulting scatter plots in Figure 2 show a general agreement of the two sets of values, but a clear bias is visible. Figure 2 highlights specific weather stations and it is apparent, especially for temperature, that there is a spatially-varying additive bias and a constant multiplicative bias parameter since the GSM outcomes from a specific weather station seem parallel to the regression line. For the other two meteorological variables, it is also clear that there is a spatially varying additive bias, but accounting for spatially-varying or time-varying multiplicative bias might also be necessary.

Figure 2 also shows that the quality of the GSM outcomes for the three variables varies. The discrepancy in the outcomes between the GSM and weather stations for the rainfall data is bigger than for the other two meteorological variables. The proposed data fusion model, which is discussed in Section 2, is able to gauge the relative quality of the GSM outcomes for the three meteorological variables.

PAGASA provided the aggregated data at the monthly level in terms of the mean temperature, mean relative humidity, and the total precipitation from January 2019 to December 2020. In particular, the GSM outcomes are simulated from an initial time of 0000 UTC. The reason for using monthly temporal scale is that we will use the model predictions as an input to an epidemiological model, particularly with the *Dengue* fever cases as the response variable, which are usually available as counts at the monthly level [38, 1]. The specific goal in this work, therefore, is to reconstruct monthly surfaces of meteorological variables, particularly temperature, relative humidity, and precipitation.

Current data fusion approaches

One statistical model for data fusion called *Bayesian melding* was proposed by [19] and discussed in [29]. The primary motivation in their work is in modelling the concentration of air pollutants and its public health implication. The Bayesian melding model is based on the assumption that all data sources are error-prone realizations of a common latent spatial process. Suppose $w_1(\mathbf{s})$ is the observed value of the quantity of interest from a station at a spatial location \mathbf{s} , and $w_2(B)$ is the realized outcome at a grid cell B for the numerical prediction model. The melding model assumes the following structure:

$$x(\mathbf{s}) = \mu(\mathbf{s}) + \xi(\mathbf{s}) \quad (1)$$

$$w_1(\mathbf{s}) = x(\mathbf{s}) + e(\mathbf{s}) \quad (2)$$

$$w_2(\mathbf{s}) = \alpha_0(\mathbf{s}) + \alpha_1(\mathbf{s})x(\mathbf{s}) + \delta(\mathbf{s}) \quad (3)$$

$$w_2(B) = \frac{1}{|B|} \int_B w_2(\mathbf{s}) d\mathbf{s} \quad (4)$$

In Equation (1), $x(\mathbf{s})$ is the latent process of interest, $\mu(\mathbf{s})$ is the mean of the process which is typically a function of fixed covariates, and $\xi(\mathbf{s})$ is a residual component which can be spatially correlated. Equation (2) links the observed outcomes at the stations $w_1(\mathbf{s})$ and the latent process $x(\mathbf{s})$. It follows the classical error model, i.e., $e(\mathbf{s}) \stackrel{\text{iid}}{\sim} \mathcal{N}(0, \sigma_e^2)$ where $e(\mathbf{s})$ is the error component. Data from the numerical forecast model is treated as a gridded data where $w_2(B)$ is the spatial average over grid cell B of a conceptual point-referenced model $w_2(\mathbf{s})$ as shown in Equation (4). Equation (3) specifies the biases in the numerical prediction model via the model components $\alpha_0(\mathbf{s})$ and $\alpha_1(\mathbf{s})$ which are interpreted as additive and multiplicative biases, respectively. It also involves another random noise component $\delta(\mathbf{s}) \stackrel{\text{iid}}{\sim} \mathcal{N}(0, \sigma_\delta^2)$. The main advantage of this specification is that it allows the two spatially misaligned data to jointly inform about the latent process $x(\mathbf{s})$. Due to model identifiability problems, $\alpha_0(\mathbf{s})$ and $\alpha_1(\mathbf{s})$ are typically parameterized as fixed effects instead of spatial random fields. In particular, $\alpha_0(\mathbf{s})$ is a polynomial function of \mathbf{s} while $\alpha_1(\mathbf{s})$ is an unknown constant.

A similar idea was proposed in [36]. Given a zero-mean process $\xi(\mathbf{s})$ with a stationary covariance function, the model for the data outcomes $w_1(\mathbf{s})$ and $w_2(B)$ is given by

$$w_1(\mathbf{s}) | \xi(\mathbf{s}) \sim \mathcal{N}\left(\mu(\mathbf{s}) + \xi(\mathbf{s}), \sigma_e^2\right) \quad (5)$$

$$w_2(B) = \frac{1}{|B|} \int_B \left(\mu(\mathbf{s}) + \xi(\mathbf{s})\right) d\mathbf{s}. \quad (6)$$

However, the model in Equation (6) does not account for the measurement error in $w_2(B)$. This is also the same model specification in [52]. Although it uses the same idea as the melding model in Equations (1) to (3) where both equations have a common latent process, it does not incorporate bias parameters such as $\alpha_0(\mathbf{s})$ and $\alpha_1(\mathbf{s})$. In a joint modelling framework, the data coming from $w_2(B)$ can dominate the parameter estimation since there are considerably more outcomes from this data source compared to $w_1(\mathbf{s})$ [29]. The calibration parameters in Equation (3) impose a restriction on this regard by accounting for higher measurement error from this data source. These calibration parameters were accounted for in [51] and they also proposed the use of the same estimation strategy as [36]. A limitation of their model is that they assumed that both $\alpha_0(\mathbf{s})$ and $\alpha_1(\mathbf{s})$ are constant in space and time. This specification may not be very flexible in calibrating the numerical forecast model.

[18] proposed another data fusion model, but instead of assuming a common single latent process for the observed outcomes, they assumed several latent processes which are shared across all the observation data. But these different latent processes do not have a clear interpretation; in fact, these processes were simply referred to as spatial random effects. For instance, suppose $w_1(\mathbf{s})$, $w_2(\mathbf{s})$, and $w_3(\mathbf{s})$ are three data sources with mean

$\mu_1(\mathbf{s})$, $\mu_2(\mathbf{s})$, and $\mu_3(\mathbf{s})$, respectively, then the proposed model is as follows:

$$\mu_1(\mathbf{s}) = \beta_1 + \xi_1(\mathbf{s}) \quad (7)$$

$$\mu_2(\mathbf{s}) = \beta_2 + \lambda_2 \xi_1(\mathbf{s}) + \xi_2(\mathbf{s}) \quad (8)$$

$$\mu_3(\mathbf{s}) = \beta_3 + \lambda_3 \xi_1(\mathbf{s}) + \lambda_4 \xi_2(\mathbf{s}) + \xi_3(\mathbf{s}) \quad (9)$$

The parameters β_1 , β_2 , and β_3 are fixed effects while $\xi_i(\mathbf{s})$, $i = 1, 2, 3$ are spatial random effects which are shared among the observational data, and with λ_j , $j = 2, 3, 4$ as unknown scaling parameters. This approach is also closely related to the so-called coregionalization model [46]. The original melding model in Equations (1) to (3) assumes a single common latent process and has a clear interpretation as the true process and that the different observation data are error-prone realizations of the process with varying levels and degree of measurement error. The model in Equations (7) to (9) deviates from this general principle.

One bottleneck with the melding model in Equations (1) to (3) is that it requires considerable computational effort because of the change-of-support integral in Equation (4). A model which tries to overcome this difficulty was proposed in [43], given by:

$$x(\mathbf{s}) = \tilde{x}(B) + \nu(\mathbf{s}) \quad (10)$$

$$w_1(\mathbf{s}) = x(\mathbf{s}) + e(\mathbf{s}) \quad (11)$$

$$w_2(B) = \alpha_0 + \alpha_1 \tilde{x}(B) + \psi(B). \quad (12)$$

$\tilde{x}(B)$ is considered as the true areal process and is defined on the same grid resolution as $w_2(B)$. The term $\nu(\mathbf{s})$ is a Gaussian error while $\psi(B)$ is a discrete spatial effect which is commonly estimated using a conditionally autoregressive model. A limitation of this model is that it considers the underlying true process as discrete and that it can only provide gridded predictions of the true process.

Another statistical approach for doing data fusion, called the regression calibration approach, fits a regression model using the outcomes of the numerical prediction model as a predictor and the observational data as the response variable. The model is given by

$$w_1(\mathbf{s}) = \alpha_0(\mathbf{s}) + \alpha_1(\mathbf{s}) w_2(B_s) + e(\mathbf{s}), \quad e(\mathbf{s}) \stackrel{\text{iid}}{\sim} \mathcal{N}(0, \sigma_e^2). \quad (13)$$

Here, $\alpha_0(\mathbf{s})$ and $\alpha_1(\mathbf{s})$ are spatially varying additive and multiplicative biases, while $w_2(B_s)$ is the value of the numerical forecast model at the grid B which contains the point location \mathbf{s} . [13] used this approach to estimate chlorophyll-A concentration over eutrophic lakes, [31] to model air quality, and in [9] to model ozone concentration. Obviously, there is a computational advantage with this approach since it only uses the values of $w_2(B)$ linked to a stations data $w_1(\mathbf{s})$ to fit the model, and then uses the full data $w_2(B)$ for predictions. A limitation of the calibration framework is that it assumes that the observed measurements $w_1(\mathbf{s})$ are the gold standard, even though it is very likely to have instrumental errors [29]. Also, since $w_2(B)$ is used as a predictor, then it cannot contain missing values. However, remote-sensed data can be missing due to cloud cover and highly reflective surfaces [29]. In addition, the resolution of the predicted latent surface for the quantity of interest depends on the resolution of $w_2(B)$. [18] performed a comparison of the melding model and the regression calibration approach in a specific data application. The results show that the Bayesian melding model gave better model predictions compared to the regression calibration approach.

Unlike the approaches discussed so far, this work accounts for calibration biases in the data fusion model, specifies a flexible bias formulation, defines a single and interpretable latent processes for the different data sources, and specifies a measurement error for the stations data. In particular, we specify a random field for the additive bias $\alpha_0(\mathbf{s})$ which we call an *error field*. Furthermore, we use a flexible specification by assuming that the error field is a time-varying random field and that α_1 is constant in space and time. Finally, our proposed model treats the outcomes of numerical prediction models as point-referenced at the centroids of the grids B , which is the same strategy as in [18, 51, 31]. A comparison between the predictions from using the proposed data fusion model, the stations-only model, and the regression calibration approach in the real data application was done using the leave-group-out crossvalidation. We also conducted a simulation study in order to assess the benefits of doing data fusion under specific scenarios.

Monte Carlo methods have been the standard approach to doing inference with Bayesian melding model [17, 48, 34, 40]. In recent years, the use of the integrated nested Laplace approximation (INLA) paired with the stochastic partial differential equations (SPDE) approach has been widely used [41, 32]. The INLA method is a deterministic approach for doing Bayesian inference for latent Gaussian models. Moreover, the SPDE method is another efficient computational method to estimate Gaussian fields of the Matérn type [32]. One challenge in

the proposed model, which is discussed in more detail in Section 2.2, is that it involves non-linear components primarily due to the α_1 multiplicative bias parameter as shown in Equation 3. To overcome this issue, we primarily use Bayesian model averaging with INLA for model inference.

Section 2 discusses the framework and the data fusion model, while section 3 discusses the model estimation approaches. Sections 4 and 5 discusses the results from a simulation study and the application to real data, respectively.

DATA FUSION FRAMEWORK AND MODEL

Framework

We assume that the process of interest is denoted by $x(\mathbf{s}, t)$ which is the true outcome at a spatial location \mathbf{s} and time t , $\mathbf{s} \in \mathcal{S}$, $t = 1, \dots, T$. This is observed via two different data sets. The first one is given by

$$\mathbf{w}_{1t}^\top = \begin{pmatrix} w_1(\mathbf{s}_1, t) & w_1(\mathbf{s}_2, t) & \dots & w_1(\mathbf{s}_{n_M}, t) \end{pmatrix}, \quad t = 1, \dots, T; \quad \mathbf{s}_i \in \mathcal{S},$$

which consists of observations from a set of n_M stations in locations \mathbf{s}_i , $i = 1, \dots, n_M$, and provides observations at time points $t = 1, \dots, T$. The second one is given by

$$\mathbf{w}_{2t}^\top = \begin{pmatrix} w_2(\mathbf{g}_1, t) & w_2(\mathbf{g}_2, t) & \dots & w_2(\mathbf{g}_{n_G}, t) \end{pmatrix}, \quad t = 1, \dots, T; \quad \mathbf{g}_j \in \mathcal{S}$$

which consists of the gridded output of a numerical model, for example the GSM model. We assume that $w_2(\mathbf{g}_j, t)$ is the value at the grid with centroid \mathbf{g}_j , $j = 1, \dots, n_G$, at time $t = 1, \dots, T$. Here we assume that the two data sources are aligned in time. If this is not the case, it is always possible to aggregate the higher resolution data. We further assume that \mathbf{w}_{2t} has a much wider spatial coverage than \mathbf{w}_{1t} ($n_M \ll n_G$) but with a larger bias, and that both \mathbf{w}_{1t} and \mathbf{w}_{2t} are error-prone realizations of the same process of interest \mathbf{x}_t . This implies that:

$$\mathbf{w}_{1t} = f_1(\mathbf{x}_t, \boldsymbol{\theta}_1) + \mathbf{e}_{1t} \quad (14)$$

$$\mathbf{w}_{2t} = f_2(\mathbf{x}_t, \boldsymbol{\theta}_2) + \mathbf{e}_{2t}, \quad (15)$$

where $f_1(\cdot)$ and $f_2(\cdot)$ are some deterministic functions of the process \mathbf{x}_t with bias parameters $\boldsymbol{\theta}_1$ and $\boldsymbol{\theta}_2$. The terms \mathbf{e}_{1t} and \mathbf{e}_{2t} are assumed independent error components. Notice that expanding the above framework to more than two data sources is straightforward as a new data set would be treated as yet another error-prone realization of the process of interest.

Proposed Model

Using Equations (14) and (15) to represent the two data sources, we propose the following data fusion model for the meteorological data:

$$x(\mathbf{s}, t) = \boldsymbol{\beta}^\top \mathbf{z}(\mathbf{s}, t) + \xi(\mathbf{s}, t) \quad (16)$$

$$w_1(\mathbf{s}_i, t) = x(\mathbf{s}_i, t) + e_1(\mathbf{s}_i, t), \quad i = 1, \dots, n_M, \quad (17)$$

$$w_2(\mathbf{g}_j, t) = \alpha_0(\mathbf{g}_j, t) + \alpha_1 x(\mathbf{g}_j, t) + e_2(\mathbf{g}_j, t), \quad j = 1, \dots, n_G. \quad (18)$$

The process of interest, $x(\mathbf{s}, t)$, is modelled as a linear function of some known covariates $\mathbf{z}(\mathbf{s}, t)$ (including an intercept) and a random field $\xi(\mathbf{s}, t)$. The observed data $w_1(\mathbf{s}_i, t)$ from the weather stations are assumed to be unbiased observation of the latent values $x(\mathbf{s}_i, t)$ with an additive error term $e_1(\mathbf{s}_i, t) \stackrel{\text{iid}}{\sim} \mathcal{N}(0, \sigma_{e_1}^2)$, $i = 1, \dots, n_M$. The iid assumption is justified by the fact that the weather stations are sparsely located in the spatial domain and operate independently of each other. The data $w_2(\mathbf{g}_j, t)$ from the numerical weather prediction model are assumed to be biased observation of the latent values $x(\mathbf{g}_j, t)$, $j = 1, \dots, n_G$. We specify both an additive and a multiplicative bias for $w_2(\mathbf{g}_j, t)$. While the multiplicative bias α_1 is assumed to be constant in time and space, the additive bias or error field $\alpha_0(\mathbf{g}_j, t)$ is a random field and also varies in time. A constant multiplicative bias is justified based on Figure 2. This is very apparent for the mean temperature since the points for the highlighted stations are strongly parallel to the line. For the other two meteorological variables, this is less apparent, and so the assumption of a constant α_1 provides an approximation of a possibly spatially-varying or time-varying α_1 . Finally, the model for $w_2(\mathbf{g}_j, t)$ contains another unstructured error $e_2(\mathbf{g}_j, t) \stackrel{\text{iid}}{\sim} \mathcal{N}(0, \sigma_{e_2}^2)$.

Both the spatio-temporal field $\xi(\cdot, t)$ in the latent process in Equation (16) and the error field $\alpha_0(\cdot, t)$ in Equation (18) are modelled using a Matérn Gaussian space-time field. In practice, we assume that

$$\xi(\mathbf{s}, t) = \phi_1 \xi(\mathbf{s}, t-1) + \omega_1(\mathbf{s}, t) \quad (19)$$

$$\alpha_0(\mathbf{s}, t) = \phi_2 \alpha_0(\mathbf{s}, t-1) + \omega_2(\mathbf{s}, t), \quad (20)$$

where $|\phi_1| < 1$ and $|\phi_2| < 1$ model the temporal dependence in an autoregressive (AR) fashion of order 1 while $\omega_1(\mathbf{s}, t)$ and $\omega_2(\mathbf{s}, t)$ are two independent Gaussian innovation processes with Matérn covariance structure, i.e.,

$$\text{Cov}(\omega_h(\mathbf{s}_i, t), \omega_h(\mathbf{s}_j, u)) = \begin{cases} 0 & t \neq u, \\ \Sigma_{i,j}^{(h)} & t = u \end{cases}, \quad (21)$$

$$\Sigma_{i,j}^{(h)} = \frac{\sigma_h^2}{2^{\nu_h-1} \Gamma(\nu_h)} (\kappa_h \|\mathbf{s}_i - \mathbf{s}_j\|)^{\nu_h} K_{\nu_h}(\kappa_h(\|\mathbf{s}_i - \mathbf{s}_j\|)), \quad (22)$$

for $h = 1, 2$. Here, $\|\cdot\|$ is the Euclidean distance in \mathbb{R}^2 between two locations \mathbf{s}_i and \mathbf{s}_j , and $K_{\nu_h}(\cdot)$ is the modified Bessel function of the second kind and order $\nu_h > 0$. The Matérn field is parameterized by the marginal variance σ_h^2 , a scaling parameter κ_h , and a smoothness parameter ν_h which is related to the mean-square differentiability of the process. The smoothness parameter is typically fixed at some value because it is poorly identified in many applications [32]. Moreover, the scaling parameter is related to the range parameter via the empirically derived relationship $\rho_h \approx \frac{\sqrt{8\nu_h}}{\kappa_h}$. Given the model structure in Equations (19) to (22), we have

$\xi_t \sim \mathcal{N}(\phi_1 \xi_{t-1}, \Sigma^{(1)})$ and $\alpha_{0t} \sim \mathcal{N}(\phi_2 \alpha_{0,t-1}, \Sigma^{(2)})$ for $t = 1, \dots, T$, where $\xi_t = (\xi(\mathbf{s}_1, t) \ \dots \ \xi(\mathbf{s}_{n_M}, t))^\top$, $\alpha_{0t} = (\alpha_0(\mathbf{g}_1, t) \ \dots \ \alpha_0(\mathbf{g}_{n_G}, t))^\top$, and that $\Sigma^{(1)}$ and $\Sigma^{(2)}$ are dense covariance matrices whose elements are given in Equation (22). Both $\xi(\mathbf{s}, t)$ and $\alpha_0(\mathbf{s}, t)$ follows the stationary distribution at time 1, i.e., $\xi(\mathbf{s}, 1) \sim \mathcal{N}(0, \sigma_1^2/(1 - \phi_1^2))$ and $\alpha_0(\mathbf{g}, 1) \sim \mathcal{N}(0, \sigma_2^2/(1 - \phi_2^2))$.

MODEL ESTIMATION

The estimation approach uses the integrated nested Laplace approximation (INLA) which is a method for doing deterministic Bayesian inference for hierarchical models which are latent Gaussian [41]. The joint model in Equations (16) to (18) is a latent Gaussian model which becomes obvious after rewriting it, in vector form, as

$$\mathbf{w}_{1t} = \mathbf{Z}_t \boldsymbol{\beta} + \xi_t + \mathbf{e}_{1t}, \quad \mathbf{e}_{1t} \sim \mathcal{N}(\mathbf{0}, \sigma_{e_1}^2 \mathbb{I}), \quad t = 1, \dots, T, \quad (23)$$

$$\xi_t = \phi_1 \xi_{t-1} + \omega_{1t} \quad (24)$$

$$\mathbf{w}_{2t} = \boldsymbol{\alpha}_{0t} + \alpha_1(\mathbf{Z}_t \boldsymbol{\beta} + \xi_t) + \mathbf{e}_{2t}, \quad (25)$$

$$\boldsymbol{\alpha}_{0t} = \phi_2 \boldsymbol{\alpha}_{0,t-1} + \omega_{2t}, \quad \mathbf{e}_{2t} \sim \mathcal{N}(\mathbf{0}, \sigma_{e_2}^2 \mathbb{I}). \quad (26)$$

The model specification involves two likelihood components: \mathbf{w}_{1t} and \mathbf{w}_{2t} . The latent part of the model includes the fixed effects $\boldsymbol{\beta}$, the space-time effects ξ_t , and the error field $\boldsymbol{\alpha}_{0t}$, $t = 1, \dots, T$. The fixed effects $\boldsymbol{\beta}$ are given a non-informative prior which is Gaussian with mean zero and a large variance, while the random fields ξ_t and $\boldsymbol{\alpha}_{0t}$ follow a Gaussian autoregressive structure as described in Equations (19) to (22). The hyperparameters include the parameters of the Matérn field ω_{1t} , particularly σ_1, ρ_1 , and ϕ_1 , and the parameters of the error field, namely σ_2, ρ_2 , and ϕ_2 . The measurement error variance parameters $\sigma_{e_1}^2$ and $\sigma_{e_2}^2$ are also considered hyperparameters. The aforementioned hyperparameters are given penalized complexity (PC) priors [20, 49]. PC priors are weakly informative priors which penalize the complexity of Gaussian random fields by shrinking the range towards infinity and the marginal variance towards zero [20]. These are defined and expressed through probability statements of the type $\mathbb{P}(\sigma > \sigma_o) = \nu_1$ and $\mathbb{P}(\rho < \rho_o) = \nu_2$, where $\nu_1, \nu_2 \in (0, 1)$ are probability values chosen by the user, while σ_o and ρ_o are also user-defined values of the parameters. The variance parameters $\sigma_{e_1}^2$ and $\sigma_{e_2}^2$ are also given PC priors.

A potential issue is that α_1 is a scaling parameter of an unknown Gaussian field, $\mathbf{Z}_t \boldsymbol{\beta} + \xi_t$. Although this violates the latent Gaussian assumption of INLA, this model specification could still be estimated in the INLA framework by doing data augmentation, which in consequence considers α_1 as a model hyperparameter [37, 35, 42, 51]. However, scaling parameters are typically difficult to estimate and the model could run into numerical issues in such a scenario. Hence, we explore in this work the use of a Bayesian model averaging (BMA) approach with INLA [23]. This approach allows us to fit the data fusion model conditional on α_1 . When α_1 is fixed, the proposed data fusion model in Equations (23) to (26) is latent Gaussian.

Fitting the data fusion model conditional on α_1 is a viable approach since we have a sensible set of values for α_1 which is on a grid centered at 1. When $\alpha_1 = 1$, this implies that there is no multiplicative bias in \mathbf{w}_{2t} ; and the further the value of α_1 is away from 1, the more serious the multiplicative bias in \mathbf{w}_{2t} .

Suppose all observed data is denoted by \mathbf{Y} , a latent model component is denoted by x_j , and the model hyperparameters are denoted by $\boldsymbol{\theta}$. INLA computes the posterior marginals based on the following nested integrals:

$$\pi(\theta_i|\mathbf{Y}) = \int \pi(\boldsymbol{\theta}|\mathbf{Y})d\boldsymbol{\theta}_{-i} \quad (27)$$

$$\pi(x_j|\mathbf{Y}) = \int \pi(x_j|\boldsymbol{\theta}, \mathbf{Y})\pi(\boldsymbol{\theta}|\mathbf{Y})d\boldsymbol{\theta}. \quad (28)$$

We express $\boldsymbol{\theta} = \begin{pmatrix} \alpha_1 & \boldsymbol{\theta}_{-\alpha_1} \end{pmatrix}^\top$, where $\boldsymbol{\theta}_{-\alpha_1}$ includes all hyperparameters excluding α_1 . In this regard, the posterior marginals in Equations (27) and (28) can be expressed as

$$\pi(\cdot|\mathbf{Y}) = \int \pi(\cdot|\alpha_1, \mathbf{Y})\pi(\alpha_1|\mathbf{Y})d\alpha_1. \quad (29)$$

The density $\pi(\cdot|\alpha_1, \mathbf{Y})$ is the marginal posterior conditional on α_1 . This conditional marginal posterior can be computed using INLA for a fixed α_1 . The density $\pi(\alpha_1|\mathbf{Y})$ in Equation (29) can be expressed as

$$\pi(\alpha_1|\mathbf{Y}) \propto \pi(\mathbf{Y}|\alpha_1)\pi(\alpha_1),$$

where $\pi(\mathbf{Y}|\alpha_1)$ is the conditional marginal likelihood and $\pi(\alpha_1)$ is the prior for α_1 . The computation is done by specifying a grid of values for α_1 , say $\alpha_1^{(k)}$, $k = 1, \dots, K$, and then fitting the INLA conditional on each $\alpha_1^{(k)}$. Given this ensemble of INLA models, the weights for model averaging are computed as:

$$w_k = \frac{\pi(\mathbf{Y}|\alpha_1^{(k)})\pi(\alpha_1^{(k)})}{\sum_{k=1}^K \pi(\mathbf{Y}|\alpha_1^{(k)})\pi(\alpha_1^{(k)})}. \quad (30)$$

The marginal posteriors given in Equation (29) are then computed as

$$\pi(\cdot|\mathbf{Y}) \approx \sum_{k=1}^K \pi(\cdot|\alpha_1^{(k)}, \mathbf{Y})w_k. \quad (31)$$

All other posterior quantities of interest and all predictions are computed using model averaging. A disadvantage of the model averaging approach is that it requires us to fit the models conditional on each α_1 value which can be inefficient especially for large spatio-temporal datasets.

Moreover, we use the stochastic partial differential equations (SPDE) approach to fit the Matérn fields in the model, particularly, ω_{1t} and ω_{2t} . The SPDE method approximates a Gaussian field with Matérn covariance function using a Gaussian Markov random field which has a sparse precision matrix and therefore allows fast model inference [32].

SIMULATION STUDY

In this section, we perform a simulation study with the aim to show that data fusion allows us to recover more accurate predictions of the latent process of interest and better estimates of model parameters. To simulate our data, we use the shapefile of the Belo horizonte region in Brazil, available in the R package *spdep* [11]. This region has a total surface area of ca 330 km². We perform the simulation study on a purely spatial context and simulate the process of interest as:

$$x(\mathbf{s}) = \beta_0 + \beta_1 z(\mathbf{s}) + \xi(\mathbf{s}) \quad (32)$$

where $\xi(\mathbf{s})$ is a Matérn random field with the following parameters: effective range $\rho_\xi = 2$ degrees, marginal standard deviation $\sigma_\xi = 3.16$, and smoothness parameter equal to 1. The value of the range is such that the spatial correlation becomes negligible at a distance of ca 222 km which corresponds to half of the maximum distance in the study region. Moreover, $z(\mathbf{s})$ is a known covariate and is simulated from a Matérn process with effective range of 3 degrees, a marginal variance of 1, and a smoothness parameter equal to 1. The fixed effects are $\beta_0 = 10$ and $\beta_1 = 3$.

The two observed datasets are simulated as follows:

$$w_1(\mathbf{s}_i) = x(\mathbf{s}_i) + e_1(\mathbf{s}_i), \quad i = 1, \dots, n_M \quad (33)$$

$$w_2(\mathbf{g}_j) = \alpha_0(\mathbf{g}_j) + \alpha_1 x(\mathbf{g}_j) + e_2(\mathbf{g}_j), \quad j = 1, \dots, n_G, \quad (34)$$

wherein the locations of the n_M weather stations are randomly distributed over the study area while the n_G numerical model values are observed on a regular grid. In the data simulation model, we set $e_1(\mathbf{s}_i) \stackrel{\text{iid}}{\sim} \mathcal{N}(0, \sigma_{e_1}^2 = .25)$ and $e_2(\mathbf{g}_j) \stackrel{\text{iid}}{\sim} \mathcal{N}(0, \sigma_{e_2}^2 = .01)$. The values of $\sigma_{e_1}^2$ and $\sigma_{e_2}^2$ are chosen based on the empirical results from the temperature model in Section 5.1. This implies that the noise in $w_2(\mathbf{g}_j)$ is mainly attributed to the error field $\alpha_0(\mathbf{g})$. The error field $\alpha_0(\mathbf{g})$ is a Matérn random field with range $\rho_{\alpha_0} = 1$, marginal standard deviation $\sigma_{\alpha_0} = 1$, and smoothness parameter of 1. The range parameter and marginal variance of $\xi(\mathbf{s})$ is chosen to be higher compared to $\alpha_0(\mathbf{g})$ based on the empirical results from the real data application discussed in Section 5. Finally, the constant multiplicative bias parameter is $\alpha_1 = 1.1$.

Figure 3a shows the dense simulation grid. Figure 3b shows a simulated “true” surface of interest while Figure 3c shows the simulated data from the numerical forecast model at a coarser resolution than the simulation grid. The centroids of the grids in Figure 3c is a coarse subset of the points in Figure 3a. The corresponding simulated bias or error field $\alpha_0(\mathbf{g})$ is shown in Figure 3d. To illustrate the difference in the severity of the biases between $w(\mathbf{s}_i)$ and $w(\mathbf{g}_j)$, we generate a specific data example from Equations (33) and (34), with $n_M = 10$ stations and with the w_2 centroids shown in Figure 3c. The point locations of the 10 stations are shown in Figure 5a. Figure 4 shows a comparison of the biases between the outcomes of $w_1(\mathbf{s}_i)$ and $w_2(\mathbf{g}_j)$. The observed data at the 10 stations closely corresponds to the truth as shown in Figure 4a. On the other hand, the outcomes of $w_2(\mathbf{g}_j)$ are more biased and also overestimates the truth because of the multiplicative bias parameter $\alpha_1 > 1$ as shown in Figure 4b. Figure 4c shows that there is a big discrepancy between the outcomes at the stations and the outcomes from the numerical prediction model at the locations of the stations. This plot is similar to Figure 2 which shows the discrepancies in the values between the two data sources for the real data application.

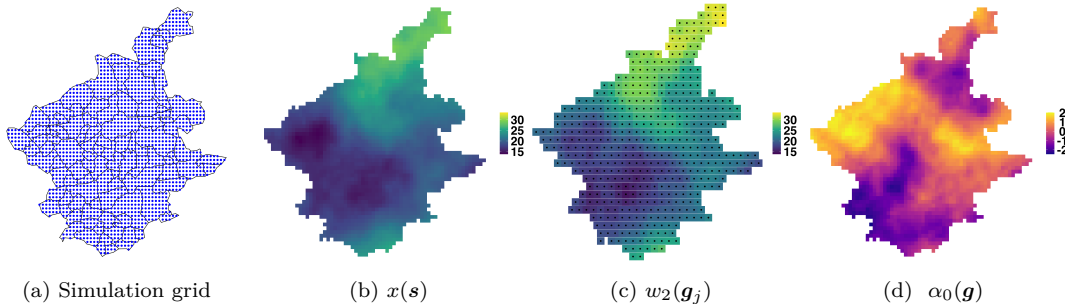


Fig. 3. (a) dense simulation grid, (b) a simulated true field $x(\mathbf{s})$, (c) a simulated outcome of the numerical model $w_2(\mathbf{g}_j)$, (d) a simulated error field $\alpha_0(\mathbf{g})$

Our main interest here is to understand if jointly modeling the two data sources offers advantages and how these change with the density or sparsity of the weather stations. We therefore consider three different cases. The first scenario consists of only $n_M = 10$ stations and with severe undersampling (Figure 5a). In the second case, we have $n_M = 25$ stations, and a large area that is undersampled (Figure 5b). The third case has $n_M = 40$ stations which are more uniformly distributed over the study area (Figure 5c). The location of the stations are held constant for all the data replicates so that the configuration of the spatial locations does not influence the results.

Model definition and estimation

We compare two approaches for estimating the latent process of interest. The first approach uses only the data from the stations and fits the following model:

$$x(\mathbf{s}) = \beta_0 + \beta_1 z(\mathbf{s}) + \xi(\mathbf{s}),$$

$$w_1(\mathbf{s}_i) = x(\mathbf{s}_i) + e_1(\mathbf{s}_i), \quad e_1(\mathbf{s}_i) \stackrel{\text{iid}}{\sim} \mathcal{N}(0, \sigma_{e_1}^2), \quad i = 1, \dots, n_M$$

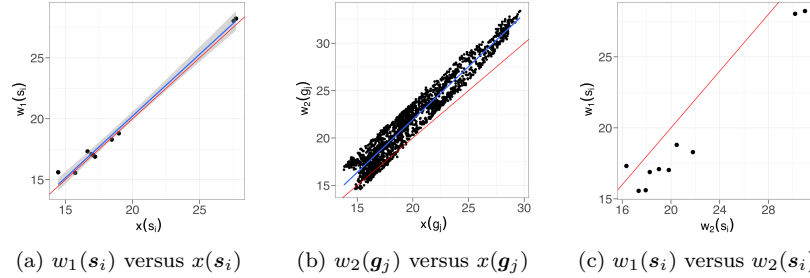


Fig. 4. (a) simulated observed values at 10 stations versus true values (b) simulated outcomes from numerical prediction model versus true values (c) simulated observed values at 10 stations versus outcomes from numerical prediction model. The simulated values for $w_2(g_j)$ are more biased than $w_1(s_i)$.

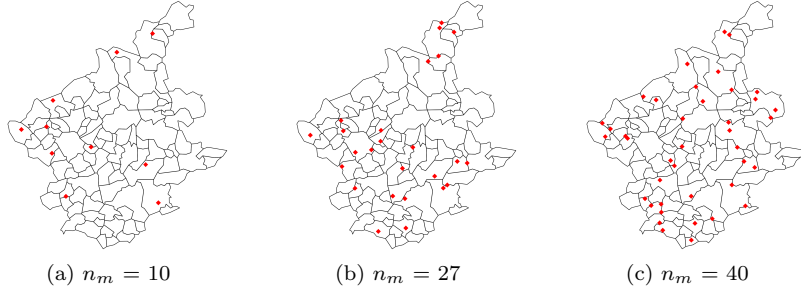


Fig. 5. Spatial location of stations over the study area: (a) a sparse network with undersampled regions, (b) a denser network but with an undersampled region, (c) a dense uniformly distributed network.

The second approach considers the two data sources and fits the following joint model:

$$\begin{aligned}
 x(\mathbf{s}) &= \beta_0 + \beta_1 z(\mathbf{s}) + \xi(\mathbf{s}), \\
 w_1(s_i) &= x(s_i) + e_1(s_i), & e_1(s_i) &\stackrel{\text{iid}}{\sim} \mathcal{N}(0, \sigma_{e_1}^2), & i &= 1, \dots, n_M \\
 w_2(g_j) &= \alpha_0(g_j) + \alpha_1 x(g_j) + e_2(g_j), & e_2(g_j) &\stackrel{\text{iid}}{\sim} \mathcal{N}(0, \sigma_{e_2}^2), & j &= 1, \dots, n_G
 \end{aligned}$$

where $\xi(\mathbf{s})$ and $\alpha_0(\mathbf{g}_j)$ are Matérn random fields with marginal standard deviations σ_ξ and σ_{α_0} and practical ranges ρ_ξ and ρ_{α_0} , respectively.

To finalize the Bayesian model, we need to specify the priors for all model parameters. We assign β_0 and β_1 a vague Gaussian prior with zero mean. We use penalized complexity (PC) priors for the variance parameters of $e_1(s_i)$ and $e_2(g_j)$ and the parameters of the two Matérn fields: ρ_ξ , σ_ξ , ρ_{α_0} , and σ_{α_0} . In this simulation experiment, we set $\nu_1 = \nu_2 = 0.5$. For the values assigned to σ_α and ρ_α , we have two scenarios. The first scenario, which we indicate as “matching priors”, uses the actual values used to simulate the datasets. The second scenario, which we call “non-matching priors”, uses $\sigma_{e_{10}} = 1.5$, $\sigma_{e_{20}} = 0.5$, $\sigma_{\xi_0} = 1$, $\rho_{\xi_0} = 0.5$, $\sigma_{\alpha_{00}} = .5$, $\rho_{\alpha_{00}} = .5$, which are arbitrarily chosen values. Note that the matching priors are not necessarily more informative than the non-matching priors and that both cases are a weakly informative specification of the priors.

We use the `inlabru` library to fit the models. The first approach which only uses the data from the stations is straightforward to fit. For the data fusion model, we use the Bayesian model averaging approach with INLA as discussed in Section 3. We define a regular grid of α_1 values centered on 1. Defining the grid around 1 is reasonable since $\alpha_1 = 1$ implies that there is no multiplicative bias in the numerical forecast model. The weights of the different models for model averaging are computed using Equation (30). We use a uniform prior for α_1 in computing the weights.

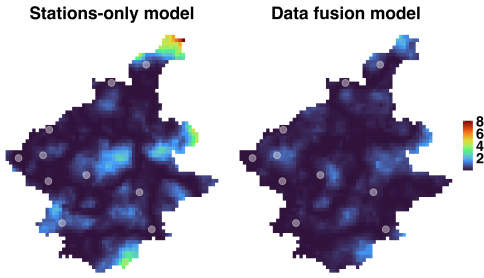


Fig. 6. Comparison of squared-errors between the stations-only model and data fusion model for the simulated data in Figure 3 and 4. The errors from the stations-only model are much higher.

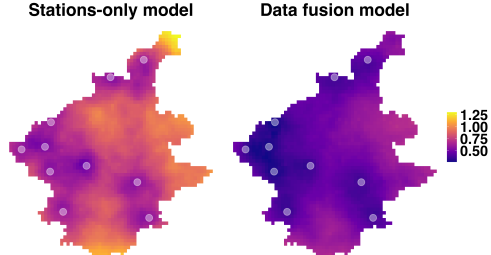


Fig. 7. Comparison of the posterior uncertainty between the stations-only model and data fusion model for the simulated data in Figure 3 and 4. The posterior uncertainty from the stations-only model are much higher.

Model assessment

We use the fitted models to estimate the values of the true process $x(\mathbf{s})$ over a set of locations \mathbf{s} which defines a prediction grid in the study domain \mathcal{S} . We used the simulation grid shown in Figure 3a as the prediction grid. The estimated value for $x(\mathbf{s})$ is the posterior mean $\mathbb{E}[x(\mathbf{s})|\mathbf{Y}]$ with uncertainty given by the posterior standard deviation $\sqrt{\mathbb{V}[x(\mathbf{s})|\mathbf{Y}]}$. Here the vector \mathbf{Y} indicates the observed data used to fit the model, so either $\mathbf{Y} = \mathbf{w}_1$ or $\mathbf{Y} = \{\mathbf{w}_1, \mathbf{w}_2\}$ for the stations-only model and the data fusion model, respectively.

We use the following metrics for model assessment:

1. Average squared error of the estimated field over \mathcal{S} : $\frac{1}{|\mathcal{S}|} \int_{\mathcal{S}} (x(\mathbf{s}) - \mathbb{E}[x(\mathbf{s})|\mathbf{Y}])^2 d\mathbf{s}$
2. Average posterior uncertainty of the estimated field over \mathcal{S} : $\frac{1}{|\mathcal{S}|} \int_{\mathcal{S}} \sqrt{\mathbb{V}[x(\mathbf{s})|\mathbf{Y}]} d\mathbf{s}$
3. Average Dawid-Sebastiani (DS) score which is a measure of the closeness between an observed quantity of interest and the prediction distribution, say \mathcal{F} . The DS score is based on a coherent design criteria and is appropriate for predictive decision problems, i.e., to predict some future observation of the process [15]. The DS score for a prediction on y is given by

$$\frac{(y - \mathbb{E}_{\mathcal{F}}(y))^2}{\mathbb{V}_{\mathcal{F}}(y)} + \log[\mathbb{V}_{\mathcal{F}}(y)], \quad (35)$$

where $\mathbb{E}_{\mathcal{F}}(y)$ and $\mathbb{V}_{\mathcal{F}}(y)$ is the mean and variance of the predictive distribution $\mathcal{F}(y)$.

The first metric is a measure of the average discrepancy between the estimated field and the true values of the latent field, $x(\mathbf{s})$, while the second metric assesses the average uncertainty in the estimated field. We approximate both integrals above using the estimated values on the prediction grid. The third metric is another proper scoring rule which depends on the predictive mean and variance of the observed data [22]. We are particularly interested in the predictions for the observational data \mathbf{w}_1 . Similar to the first two metrics, a lower value for the average DS score is preferred. We also look at the accuracy of the parameter estimates by computing the relative error and the posterior uncertainty. All simulation results are computed based on 600 independent data replicates.

Simulation study results

Figures 6 and 7 show a comparison of the squared-errors and the posterior uncertainty in an estimated field, respectively, between the stations-only model and the data fusion model on the data example in Figure 3 and 4. The spatial location of the stations are shown as white points in Figures 6 and 7. The squared errors from the stations-only model, shown in Figure 6, are generally much larger than the squared errors from the data fusion model. The posterior uncertainty of the latent field is also much larger for the stations-only model as shown in Figure 7. Also, as expected, the posterior uncertainty at the location of the stations is lower than elsewhere, which is very apparent for the stations-only model. The average squared error for the stations-only model and

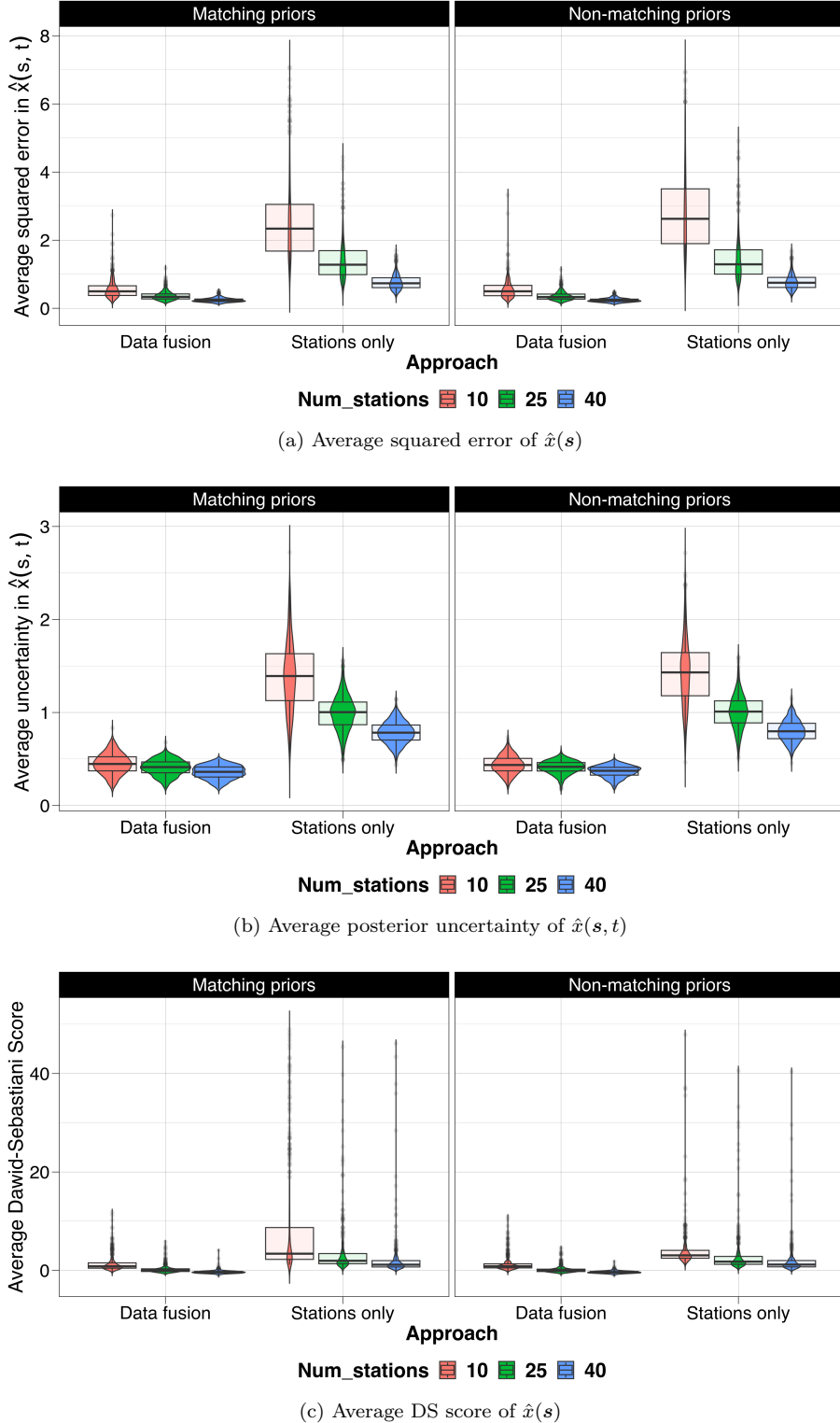


Fig. 8. Plots of the (a) average squared-errors, (b) average posterior uncertainty, and (c) average DS score from the 600 simulated datasets with respect the sparsity of the number of stations, the priors used, and the use of either stations-only model or data fusion model. The errors and the posterior uncertainty for the data fusion model is smaller especially for the case of sparse data from the stations. The DS score is also smaller on the average for the data fusion model.

data fusion model for this specific case is 0.53 and 0.27, respectively, while the average posterior uncertainty is 0.80 and 0.48, respectively. The average DS scores are 1.02 and -0.65, respectively.

Figure 8a shows a plot of the average squared errors of the estimated latent field over \mathcal{S} based on the 600 data replicates for the different simulation scenarios. The data fusion approach clearly gives smaller average squared errors, especially when the data on the stations is very sparse. The same plot also shows a comparison of the average squared errors between the use of matching and non-matching priors. The results show that there is no substantial difference with respect to the priors. Figure 8b shows the results for the average posterior uncertainty. It shows that the data fusion approach also gives lower uncertainty estimates and that higher number of stations is associated with smaller uncertainty. In addition, the same figure shows that there is no difference in the average posterior uncertainty between the use of matching and non-matching priors. Finally, Figure 8c shows the average DS scores. The average DS scores are also smaller with the data fusion approach. Furthermore, it also shows that the average DS scores tend to decrease with the number of stations, and that the use of either matching or non-matching priors gives roughly the same values on the average.

Figure 9 shows a comparison of the average relative error and average posterior uncertainty for two model hyperparameters: the marginal standard deviation of the spatial field $\xi(\mathbf{s})$ (in Figure 9a), and the standard deviation of the measurement error in the stations $e_1(\mathbf{s})$ (in Figure 9b). There is a clear benefit from doing data fusion for all scenarios, especially when the data from the stations is very sparse. The average relative errors are generally smaller when matching priors are used. The average relative error tends to decrease with more stations, especially for the stations-only model. Figures 19 and 20 in Appendix section A.1 shows the results for the fixed effects, β_0 and β_1 , and the the range parameter of the spatial field $\xi(\mathbf{s})$, respectively. The results show that the average relative error and average posterior uncertainty are also smaller for the data fusion approach. Also, the errors and the uncertainty in the estimates from the stations-only model is higher when the number of stations is very sparse. For ρ_ξ , the use of matching priors seem to give higher relative errors compared to the use of non-matching priors.

Finally, Figure 21 in Appendix section A.1 shows a summary of the model averaging weights of the INLA models for each α_1 value. The weight for $\alpha_1 = 1.1$ is the highest for all the scenarios. Moreover, the weights decrease as the value of α_1 goes further away from 1.1. The use of either matching or non-matching PC priors does not seem to substantially affect the weights.

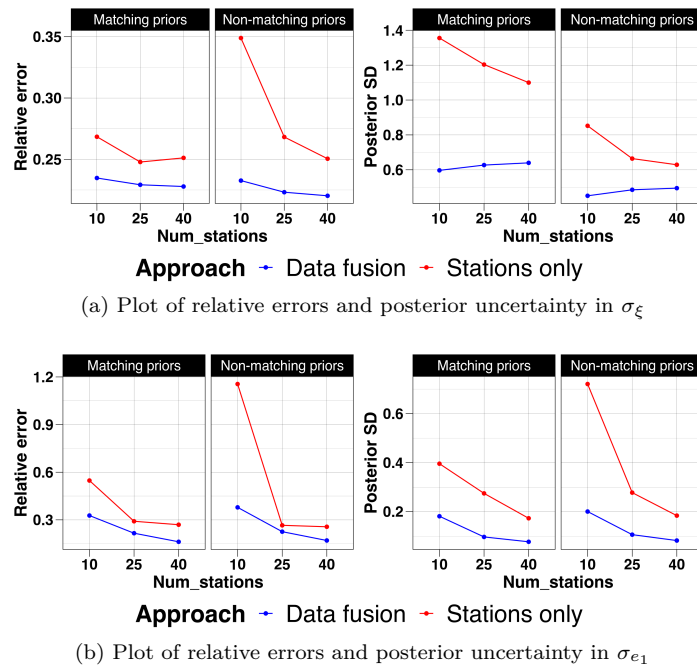


Fig. 9. Plot of average relative errors and average posterior uncertainty from 600 simulated datasets for two hyperparameters: (a) marginal standard deviation of the spatial field, σ_ξ and (b) standard deviation of measurement error at the stations, σ_{e_1} .

RESULTS FOR METEOROLOGICAL DATA FROM THE PHILIPPINES

This section presents in detail the results of the proposed data fusion model applied to meteorological data in the Philippines. Section 5.1, 5.2, 5.3 discuss the results for temperature, relative humidity, and rainfall, respectively, while section 5.4 presents the results of the leave-group-out cross-validation.

Temperature

In modelling temperature, we have the following form for the fixed effects in the latent process:

$$\text{Temperature}(\mathbf{s}, t) = \beta_0 + \beta_1 \log(\text{Elevation}(\mathbf{s}, t)) + \beta_2 \text{Cool} + \beta_3 \text{ClimateType} \quad (36)$$

There are two prevailing seasons in the Philippines: rainy or dry season [39]. Rainy season lasts from June to November, while the rest of the year is generally considered dry. The rainy season is also considered a hot episode in the country. On the other hand, the dry season is further categorized into either a cool dry or a hot dry period, where the former lasts from December to February and the latter from March to May. Hence, we define the ‘Cool’ variable in Equation (36) as a binary variable which takes a value of ‘1’ for months December to February and a value of ‘0’ for the other months. The climate type variable is also a binary variable which takes ‘1’ for the eastern section of the country and ‘0’ for the western section. The eastern part of the country is characterized as having no distinct wet or dry season and with relatively high rainfall all year round. On the other hand, most of the western section of the country are characterized as having pronounced dry and wet seasons [7].

Penalised complexity (PC) priors are used for the Matérn field parameters [20, 49]. The parameter values for the Matérn PC priors are as follows: $\rho_{1o} = \rho_{2o} = 300$ km, $\sigma_{1o} = 0.07$, $\sigma_{2o} = 0.01$. The value for the range parameters is one-third the maximum distance of the spatial domain. The value for σ_{1o} is the standard deviation of the temperature values, while the value of σ_{2o} is chosen to be some value smaller than σ_{1o} based on preliminary model results. The variance parameters of $e_1(\mathbf{s}_i, t)$ and $e_2(\mathbf{g}_j, t)$ are also given PC priors, with $\sigma_{e_{1o}} = 0.2$ and $\sigma_{e_{2o}} = 0.01$. The probability value of all PC priors is set to be equal to 0.50. The rest of the model parameters are given the default non-informative priors.

We define a grid of values from 0.5 to 1.5 with a length step of 0.1 for the multiplicative bias parameter, α_1 . A uniform prior was used for α_1 . An ensemble of INLA models were fitted for a fixed α_1 , and the BMA weights are computed using Equation 30. The marginal log-likelihoods $\log \pi(\mathbf{Y}|\alpha_1^{(k)})$ and the corresponding BMA weights w_k are shown in Appendix A.2 Table 4. The results show that the weight of the model with $\alpha_1 = 1$ is approximately equal to 1, while the rest of the models do not have a significant contribution in the model averaging.

Table 1. Posterior estimates of fixed effects for the temperature model – stations-only model versus proposed data fusion model

Parameter	Stations only				Data fusion			
	Mean	SD	P2.5%	P97.5%	Mean	SD	P2.5%	P97.5%
β_0	28.6644	2.6296	23.5104	33.8184	28.9186	4.6029	19.8972	37.9401
β_1 , log(Elevation)	-0.6308	0.0942	-0.8154	-0.4462	-0.7085	0.0506	-0.8076	-0.6093
β_2 , Cool	-0.6830	0.1982	-1.0715	-0.2946	-0.6178	0.1769	-0.9645	-0.2712
β_3 , Climate Type	2.1827	0.6991	0.8126	3.5529	0.6062	0.3367	-0.0536	1.2661

Shown in Table 1 are the posterior estimates of the fixed effects for the stations-only model and the proposed data fusion model. The estimated fixed effects for both models are quite similar, except for the climate type variable which is significant in the stations-only model but not in the proposed data fusion model. The uncertainty in the estimates for β_1 , β_2 , and β_3 are smaller for the data fusion model as expected. Elevation is negatively associated with temperature, i.e., it is colder at higher elevation. The ‘Cool’ binary variable is negatively associated with temperature, i.e., colder months (December, January, and February) have lower mean temperature compared to the rest of the months. The climate type variable is positively associated with temperature, which means that areas which are located in the eastern section of the country are warmer on the average than areas in the western section of the country.

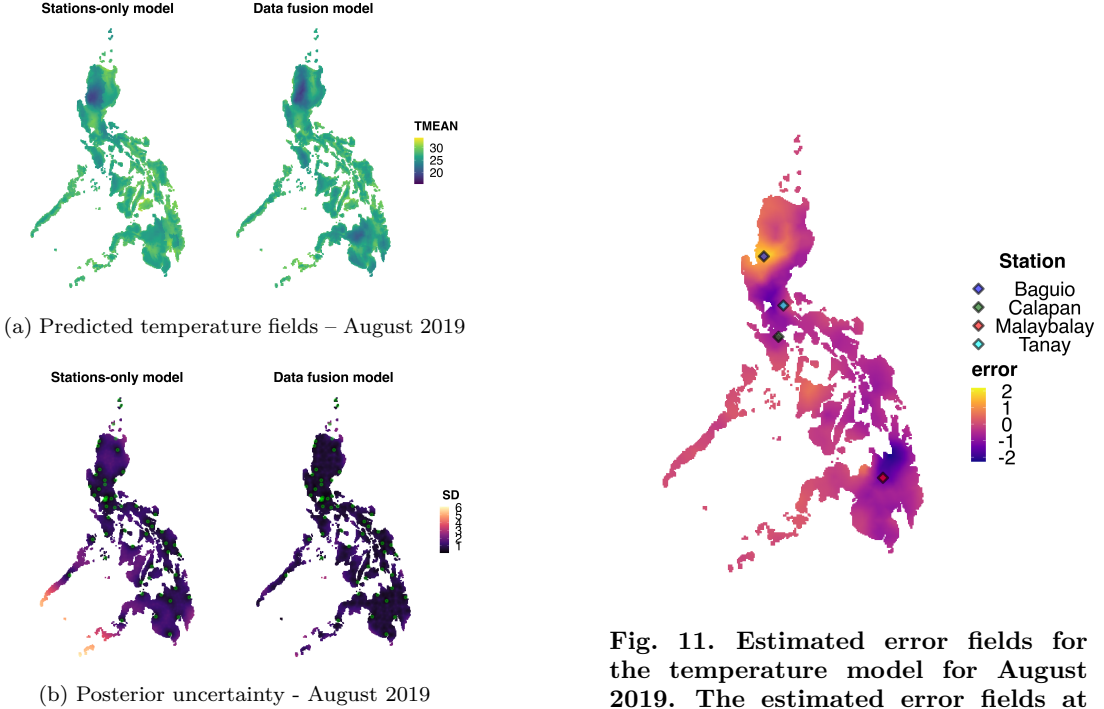


Fig. 10. Comparison of the estimated temperature fields and corresponding posterior uncertainties for August 2019 between the stations-only model and the proposed data fusion model. The posterior uncertainties from the proposed data fusion model are substantially smaller.

The posterior estimates of the hyperparameters from the stations-only model and the proposed data fusion model are also quite similar (see Table 5 in Appendix section A.2). In the data fusion model, the range parameter ρ_1 of the spatial field is higher than the range parameter ρ_2 of the error field. This means that the spatial field $\xi(s, t)$ is smoother than the error field $\alpha_0(g, t)$. The spatial correlation in the temperature spatial field and the error field becomes negligible at a distance of around 765 km and 113 km, respectively. Also, the marginal standard deviation σ_1 of the spatial field is much larger than that of the error field σ_2 . The autocorrelation parameters ϕ_1 and ϕ_2 in both the spatial field and error field are close to 1 which suggests a high degree of dependence in time.

Figure 10a shows a comparison of the estimated temperature fields for August 2019 between the stations-only model and the proposed data fusion model. The estimated fields look very similar, although the estimated field from the data fusion model is smoother. The dark spot in the northern part of the country is primarily mountainous which makes it cooler than the other parts of the country. Figure 10b shows the corresponding uncertainty estimates or standard deviation (SD) in the predicted fields. As expected, the standard deviations are smaller at the locations of the weather stations (in green points) which is more apparent for the stations-only model. Also, there is more uncertainty in the predictions from the stations-only model especially in the islands in the lower left portion. The average of the posterior standard deviation of the estimated fields from using the stations-only model and data fusion model is 1.2388 and 0.7711, respectively. Figures 22 in Appendix section A.2 shows the estimated spatial fields, $\xi(s, t)$, for the stations-only model and data fusion model for the same month. The spatial structure looks quite similar as the estimated temperature fields in Figures 10a.

Figure 11 shows the estimated error field $\hat{\alpha}_0(g_j, t)$ for the GSM data for the same month, August 2019. We can relate this plot with Figure 2 which shows the discrepancies in the values between the weather stations and the GSM outcomes. From Figure 11, the estimated error outcomes around the neighborhood of Baguio station (in blue) is the highest, i.e., the GSM has overestimated the temperature value in this area. This is consistent with Figure 2, which shows that the GSM outcomes are larger than the observed data at the station. Similarly, the estimated error values in the neighborhood of Malaybalay station (in red) is negative, and is consistent with

Fig. 11. Estimated error fields for the temperature model for August 2019. The estimated error fields at the specific stations correspond to the additive bias shown in Figure 2.

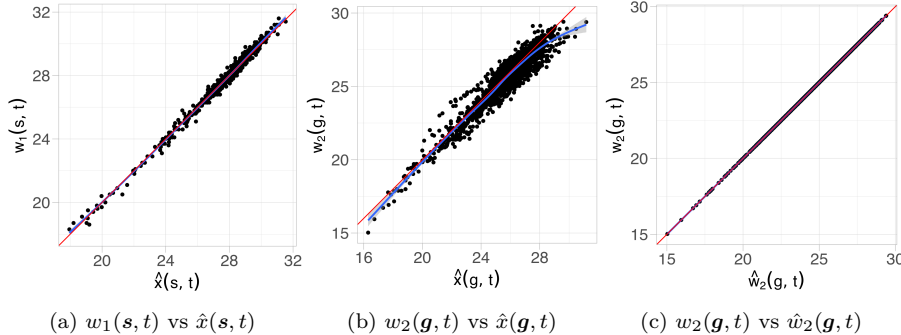


Fig. 12. Plot of observed temperature values versus predicted values using the proposed data fusion model for (a) weather stations, (b) GSM data, and (c) calibrated GSM data

Figure 2, which shows that there is a negative bias in the outcomes from the GSM in this area. For Tanay station (in cyan), the estimated error is around zero which is also expected since Figure 2 shows that there seems to be no additive bias in the GSM outcomes.

We also explored the regression calibration approach for doing data fusion which uses the GSM outcomes as a predictor in the model, as explained in Equation (13). The model estimates are shown in Appendix A.2 Table 6. The corresponding predicted temperature field for August 2019, the posterior uncertainty, and the estimated spatial field for the same month are shown in Appendix A.2 Figure 23. The results from the regression calibration approach are quite similar to the stations-only model. The proposed data fusion model has the smallest posterior uncertainty among the three approaches. A better comparison of the three approaches is discussed in section 5.4 which shows the cross-validation results.

Figure 12a shows a scatterplot between the observed values at the stations $w_1(s_i, t)$ and the corresponding predicted latent values $\hat{x}(s_i, t)$ using the proposed data fusion model. The plot shows a close correspondence between the two sets of values. Figure 12b, which shows a scatter plot between the observed GSM values $w_2(g_j, t)$ and the corresponding predicted latent values, indicates a strong bias in the GSM values, with several points that are either overestimated or underestimated. Finally, Figure 12c shows a scatter plot between the observed GSM data $w_2(g_j, t)$ and the predicted values $\hat{w}_2(g_j, t) = \hat{\alpha}_0(g_j, t) + \hat{\alpha}_1 x(g_j, t)$, indicating a very close correspondence between the two values. This shows that the error field can be effectively used to calibrate the GSM outcomes for temperature.

Relative Humidity

In modelling relative humidity (RH), we have the following form for the fixed effects in the latent process:

$$\log(RH(s, t)) = \beta_0 + \beta_1 \log \text{Temp}(s, t) + \beta_2 (\log \text{Temp}(s, t))^2 + \beta_3 \log(\text{Elevation}(s, t)) + \beta_4 \text{ClimateType} \quad (37)$$

Elevation and climate type are also used as predictors for the relative humidity model. In addition, we use log temperature and its quadratic term as a predictor in the model as recommended by [39]. This non-linear relationship is also established in the atmospheric science literature [24]. A log transformation on temperature is possible in the data since the range of its values for the Philippines which is a tropical country is from 16°C to 32°C. This is also done in the literature, such as in [44]. In particular, we use the predictions from the temperature model in Equation (36), in both the locations of the weather stations and the point locations of the GSM outcomes, as the input in the linear predictor in Equation (37).

PC priors are used for the Matérn field parameters. The values used to define the Matérn PC priors for the two range parameters are the same as the temperature model ($\rho_{10} = 300, \rho_{20} = 50$). For the marginal standard deviations of the fields, we have $\sigma_{10} = 0.08$ and $\sigma_{20} = 0.01$. The former is the standard deviation of the log-transformed relative humidity values, while the value of σ_{20} is chosen to be some value smaller than σ_{10} . The variance parameters of $e_1(s_i, t)$ and $e_2(g_j, t)$ are also given PC priors, with $\sigma_{e_{10}} = 0.01$ and $\sigma_{e_{20}} = 0.004$. The probability value in the PC priors are also set equal to 0.5. The rest of the model parameters are given the default non-informative priors.

From the model averaging results, the model with $\alpha_1 = 1$ also gave the highest marginal log-likelihood value and with a weight close to 1. The marginal log-likelihoods $\log \pi(\mathbf{Y} | \alpha_1^{(k)})$ and the corresponding BMA weights w_k are shown in Appendix A.3 Table 7. Table 2 shows the estimates of the fixed effects for the stations-only

model and the proposed data fusion model. The posterior means of the fixed effects from the two approaches are comparable, although the climate type variable is not significant in the stations-only model. The estimates of the hyperparameters are shown in Appendix A.3 Table 8.

Table 2. Posterior estimates of fixed effects for the relative humidity model - stations-only model versus proposed data fusion model

Parameter	Stations only				Data fusion			
	Mean	SD	P2.5%	P97.5%	Mean	SD	P2.5%	P97.5%
β_0	4.4506	0.0299	4.3920	4.5091	4.4505	0.0499	4.3526	4.5484
$\beta_1, \log(\text{Temp})$	0.5665	0.0480	0.4725	0.6606	0.7900	0.0386	0.7143	0.8656
$\beta_2, \log(\text{Temp})^2$	-0.1732	0.0144	-0.2014	-0.1450	-0.2374	0.0115	-0.2599	-0.2149
$\beta_3, \log(\text{Elevation})$	-0.0079	0.0029	-0.0135	-0.0022	-0.0131	0.0017	-0.0165	-0.0098
$\beta_4, \text{Climate Type}$	0.0282	0.0179	-0.0070	0.0634	0.0259	0.0085	0.0092	0.0426

Table 2 shows that there is a significant non-linear relationship between temperature and relative humidity. There is a positive correlation between the two variables for lower temperature values, but a negative correlation for high temperature values. The elevation variable is negatively associated with relative humidity. Moreover, the climate type variable is positively related with relative humidity which means that the areas in the eastern section of the country have higher relative humidity on the average than the western section. Similar to the results of the temperature data fusion model, the estimate of the range parameter ρ_1 of the spatial field in the latent process $\xi(s, t)$ is larger than the range parameter ρ_2 of the error field $\alpha_0(s, t)$ (see Appendix A.3 Table 8). The spatial correlation in the relative humidity values becomes negligible at a distance of around 589 km, while the spatial correlation in the error field decays to a negligible value at a distance of 117 km. Moreover, the spatial variance of the spatial field is larger than that of the error field. The estimates of the AR parameter are both close to 1, although the estimated value of the parameter for the spatial field is higher than that of the error field.

Figures 13a and 13b show the estimated relative humidity fields for two different months, August 2019 and January 2020, using the proposed data fusion model and the stations-only model, respectively. These two specific months were chosen since August is characterized as a rainy month while January is considered a dry month [39]. The spatial structure in the predicted fields between the proposed data fusion model and the stations-only model is similar, although it is apparent that there is more smoothing in the estimates from the stations-only model. Figures 13a and 13b show that in the eastern section of the country, the level of relative humidity is similar for the two months. In the western section, particularly in the northwestern section, relative humidity is very high during August, which is a rainy month, and is very low during January, which is a dry month.

Figure 14 shows the uncertainty estimates of the estimated relative humidity fields in Figure 13. As expected, there is more uncertainty in the predictions from the stations-only model. The average of the posterior standard deviation in the predicted fields from using the stations-only model and the proposed data fusion model is 0.0394 and 0.0220, respectively. Also, the uncertainty estimates are smaller at the location of the weather stations shown in green points.

Figures 24 and 25a in Appendix A.3 show the estimated spatial field of the latent process, $\xi(s, t)$, for the same two months using the stations-only model and the proposed data fusion model, respectively. The same spatial patterns observed in the estimated relative humidity field as shown in Figure 13 are also evident in the estimated spatial fields. The spatial effects for the eastern part of the country are fairly constant for the two different months, although there is a slight increase in the values for the northeastern parts during August which is a rainy month. On the other hand, the spatial effects for the western part are higher during August and lower during January. Figure 25b in Appendix A.3 shows the estimated error fields for the GSM outcomes on relative humidity for the same two months.

A regression calibration modelling approach was also explored for relative humidity. The model estimates are shown in Appendix A.3 Table 9. The estimated relative humidity fields for August 2019 and January 2020 are shown in Appendix A.3 Figure 27. The same spatial structure observed from Figure 13 are also observed from the estimated fields using the regression calibration approach. The corresponding posterior uncertainty and the estimated spatial fields for the same two months are shown in Appendix A.3 Figure 28. Similar to the results

for temperature, the estimated relative humidity fields and the corresponding posterior uncertainty using the regression calibration approach are quite similar to the stations-only model. The proposed data fusion model gave the smallest posterior uncertainty among the three approaches. The results from the cross-validation, which is a better way of doing model comparison, are discussed in section 5.4.

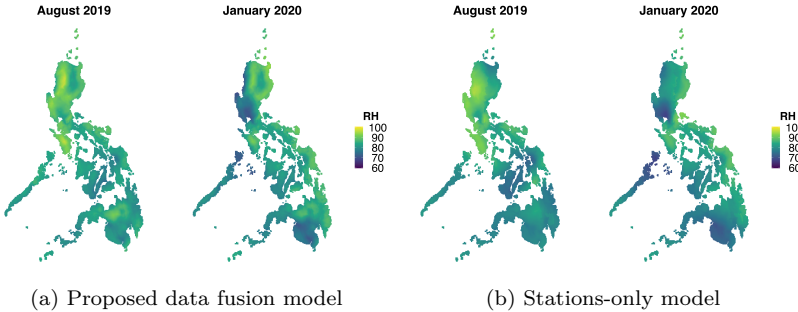


Fig. 13. Comparison of estimated relative humidity fields for August 2019 and January 2020 between (a) proposed data fusion model and (b) stations-only model. The spatial structure in the fields from the two approaches are similar. There is more smoothing in the estimated fields using the stations-only model.

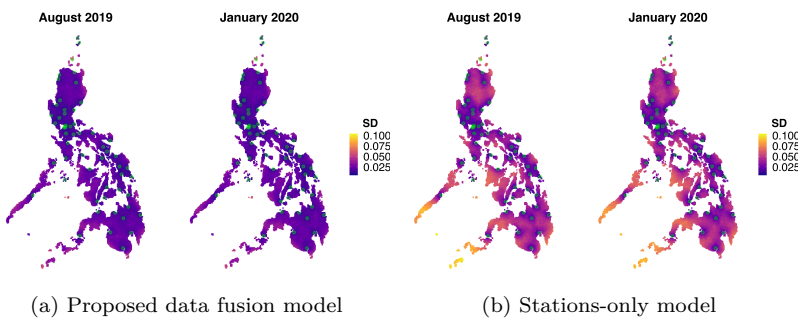


Fig. 14. Posterior uncertainty of the estimated relative humidity fields in Figure 13. The posterior uncertainty in the estimated field from using the stations-only model is much higher.

Figure 26a in the Appendix section A.3 shows a scatterplot between the observed values at the stations, $w_1(s_i, t)$, and the corresponding predicted values, $\hat{x}(s_i, t)$. There is a strong correspondence between the two values, although there are slight over- and underestimation. Figure 26b (Appendix section A.3) shows the scatter plot between the outcomes from the GSM, $w_2(g_j, t)$, and the predicted latent values, $\hat{x}(g_j, t)$. The plot shows a clear bias in the GSM outcomes. Lastly, Figure 26c (Appendix section A.3) shows a plot of the observed GSM outcomes, $w_2(g_j, t)$, and the corresponding predicted values $\hat{w}_2(g_j, t) = \hat{\alpha}_0(g_j, t) + \hat{\alpha}_1 \hat{x}(g_j, t)$. The plot shows a very close correspondence between the two values. Similar to the temperature model, the scatter plot shows that the estimated error fields can be effectively used to calibrate the GSM outcomes.

Rainfall

In modelling rainfall, the fixed effects in the latent process are as follows:

$$\log(\text{Rainfall}) = \beta_0 + \beta_1 \log \text{Temp}(s, t) + \beta_2 (\log \text{Temp}(s, t))^2 + \beta_3 \text{Season} + \beta_4 \text{ClimateType} + \beta_5 \text{ClimateType} \times \text{Season} \quad (38)$$

The ‘Season’ variable is binary which takes a value of ‘1’ for months June to November (characterized as a wet period), and a value of ‘0’ for the rest of the months which is the dry season in the country. Just like the relative humidity model, the log temperature and its squared term are also predictors in the rainfall model as

recommended by [39]. We also used the predictions from the temperature model in Equation (36) as the input in the linear predictor in Equation (38). An interaction effect between climate type and season was considered to capture the climate dynamics of the country, also as recommended by [39].

Similar to the previous models, PC priors are used for the Matérn field parameters. The same values from previous models are used to define the PC priors for the range parameters ρ_1 and ρ_2 . For the marginal standard deviations, we have $\sigma_{1o} = 1.35$, which is the standard deviation of the log-transformed rainfall values; and $\sigma_{2o} = 0.01$, which is the same for the previous models. The variance parameters of $e_1(s_i, t)$ and $e_2(g_j, t)$ are also given PC priors, with $\sigma_{e_{1o}} = 0.5$ and $\sigma_{e_{2o}} = 0.26$. The probability value in the PC priors is equal to 0.5. The rest of the model parameters are given the default non-informative priors.

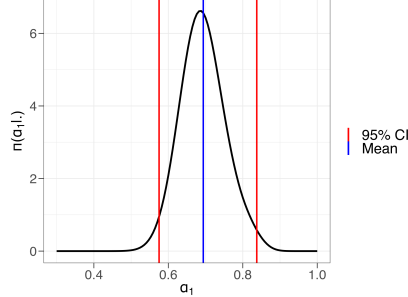


Fig. 15. Estimated marginal posterior of α_1 , $\pi(\alpha_1|Y)$, for the rainfall data fusion model. The posterior mean is 0.6733, while the 95% credible interval estimate is (0.5607, 0.8353).

Shown in Figure 15 is the estimated marginal posterior distribution of α_1 , $\pi(\alpha_1|Y)$. The posterior mean is 0.6733 while the 95% credible interval estimate is (0.5607, 0.8353). Unlike the previous two meteorological variables, the multiplicative bias parameter for the GSM outcomes for rainfall is significantly different from 1, which implies a more severe bias for rainfall outcomes. This is expected since Figure 2 shows a big discrepancy between the interpolated GSM outcomes at the locations of the weather stations and the observed values at the weather stations. This also agrees with the insights from the LGOCV results discussed in Section 5.4.

Table 3 shows the estimates of the fixed effects for the stations-only model and the proposed data fusion model. The results show that log temperature has a non-linear association with log rainfall amounts. The correlation is positive for small values of log temperature and is negative for large log temperature values. Moreover, there is a significant interaction between season and climate type. In particular, the results show that the western section of the country has a pronounced dry and wet season. On the other hand, the eastern section of the country has a less pronounced dry and wet season and with more or less evenly distributed rainfall the whole year. This can be confirmed in Figures 16a and 16b which shows the predicted log rainfall fields using the proposed data fusion model and stations-only model, respectively, for two months - August 2019 (rainy month) and January 2020 (dry month). This climatic pattern is consistent with theory [7]. Also, these are the same seasonal dynamics observed for relative humidity. The uncertainty estimates of the fields are shown in Figure 29 in Appendix A.4. The log rainfall fields from the two approaches look quite similar but the uncertainty in the predictions from the proposed data fusion model is substantially smaller as expected. The estimated spatial fields and error fields for the same two months using the proposed data fusion model are shown in Figures 31a and 31b in Appendix A.4, respectively, while Figure 30 in Appendix A.4 shows the estimated spatial fields $\xi(s, t)$ for the stations-only model.

Table 10 in Appendix A.4 shows the estimates of the hyperparameters for both the stations-only model and the proposed data fusion model. Similar to the previous meteorological variables, the estimated range ρ_1 of the spatial field in the latent process is larger than the estimated range ρ_2 of the error field. This is also true for the estimated marginal variances of the two fields. The estimated autocorrelation parameters of the two fields are very different, with the AR parameter for the error field being much larger.

A regression calibration modelling approach was also explored for rainfall. The model estimates are shown in Appendix A.4 Table 11. The predicted log rainfall fields for August 2019 and January 2020 are shown in Appendix A.4 Figure 33. The same spatial structure observed from Figures 16a and 16b are also observed from Figure 33. The estimated log rainfall fields and the corresponding posterior uncertainty using the regression calibration approach (see Figure 33 and 34 in Appendix A.4) are similar to the stations-only model. Although the proposed data fusion model gave the smallest posterior uncertainty among the three approaches, a better comparison are shown in the LGOCV results which are discussed in section 5.4.

Table 3. Posterior estimates of fixed effects for the rainfall model - stations-only model versus proposed data fusion model

Parameter	Stations only				Data fusion			
	Mean	SD	P2.5%	P97.5%	Mean	SD	P2.5%	P97.5%
β_0	4.4272	0.3598	3.7221	5.1323	4.7589	0.3771	3.9310	5.4842
β_1 , log(Temp)	2.1863	0.4541	1.2963	3.0763	1.6722	0.4297	0.9110	2.5408
β_2 , log(Temp) ²	-0.6989	0.1339	-0.9613	-0.4366	-0.5703	0.1217	-0.8090	-0.3536
β_3 , Season	0.7948	0.3061	0.1949	1.3948	0.4438	0.2610	-0.0196	0.9732
β_4 , Climate Type	1.1831	0.1456	0.8977	1.4686	0.6572	0.1119	0.4577	0.8730
β_5 , Climate Type \times Season	-0.8441	0.1617	-1.1611	-0.5271	-0.2868	0.0994	-0.4607	-0.1055

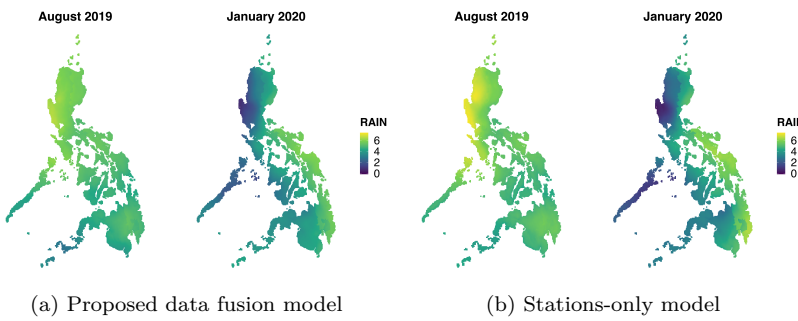
**Fig. 16.** Comparison of estimated log rainfall fields for August 2019 (wet season) and January 2020 (dry season) between (a) proposed data fusion model and (b) stations-only model. The figures show that the western section of the country has a pronounced dry and wet season.

Figure 32a in Appendix A.4 shows a scatter plot of the observed log rainfall outcomes and the predicted values at the weather stations, i.e., $w_1(\mathbf{s}, t)$ versus $\hat{x}(\mathbf{s}, t)$. The deviation between the values, especially for small log rainfall values, is large. The scatter plot between $w_2(\mathbf{g}, t)$ and $\hat{x}(\mathbf{g}, t)$, as shown in Figure 32b in Appendix A.4, shows the severe bias in the GSM outcomes. The bias is also higher for small log rainfall values. Finally, Figure 32c in Appendix A.4 shows a scatter plot of the observed GSM log rainfall data versus the predicted values calibrated by the error field, i.e., $w_2(\mathbf{g}, t)$ versus $\hat{\alpha}_0(\mathbf{g}, t) + \hat{\alpha}_1 \hat{x}(\mathbf{g}, t)$. The plot shows that there is a close correspondence between the two.

Leave-group-out cross-validation

This section presents the results of the leave-group-out cross-validation (LGOCV). The LGOCV is a better alternative than the leave-one-out cross-validation for structured models which includes multi-level models, time series models, and spatial models [33, 2]. We usually use the spatial models to do an extrapolation task, i.e., to predict on a spatial location far away from the observations' locations. The LGOCV approach is appropriate to evaluate such models since it makes the unobserved data as represented by the validation set or hold-out set less dependent on the observed data which is represented by the training set.

[33] proposed an approximation of the LGOCV for INLA models. They also proposed an automatic group construction for doing LGOCV. In this work, we manually define the groups and use a strategy tailored to the application. When making a prediction at a particular location, which is called the testing point, we leave-out that point and also all the observations within its proximity which altogether are referred to as the leave-out set. This is illustrated in Figure 17. The leave-out set consists of all the points within the circle, while the training set consists of all the points excluding the leave-out set. The testing point is technically considered part of the leave-out set, and then we predict the value at the testing point.

We use each weather synoptic station \mathbf{s}_i as a testing point. Suppose $I_{\mathbf{s}_i}$ is the leave-out set, which consists of the testing point \mathbf{s}_i and all weather stations located within a given radius from the testing point. Also,

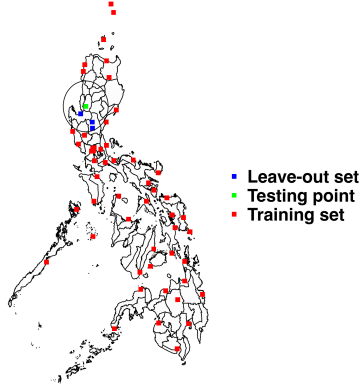


Fig. 17. Illustration of the LGOCV approach. We fit the model on the training set (red) after excluding the leave-out set (blue and green), and then make predictions on the testing point (green).

suppose $-I_{s_i}$ is the training set. The predicted value at a testing point s_i is the mean of the posterior predictive distribution $\pi(x(s_i, t) | \mathbf{Y}_{-I_{s_i}})$. To compare the competing models, we look at different posterior prediction scores. We primarily look at the Dawid-Sebastiani score whose formula is given in Equation (35). Since there are several leave-out sets, we compute the mean Dawid-Sebastiani scores (MDS) for all testing points. We also compute the root mean squared error (RMSE), mean absolute error (MAE), and the mean absolute percentage error (MAPE) of the predictions. In addition, we look at the standard deviation of $\pi(x(s_i, t) | \mathbf{Y}_{-I_{s_i}})$ and the Kullback-Leibler divergence (KLD) between $\pi(x(s_i, t) | \mathbf{Y}_{-I_{s_i}})$ and $\pi(x(s_i, t) | \mathbf{Y})$, where the latter is simply the posterior predictive distribution given the complete data and the former is the posterior predictive distribution with the data excluding the leave-out set. Since there are several leave-out sets, we compute the mean standard deviation (MSD) and the mean Kullback-Leibler divergence (MKLD) for all testing points. We look into different sizes of the leave-out set by varying the radius of the circle around the testing point. We considered four values for the radius of the leave-out set: 60, 80, 125, and 150 km.

We compare three models: the stations-only model, the regression calibration approach which is described in Equation (13), and the proposed data fusion model. Figure 18 shows a comparison of the posterior prediction scores for the temperature model. The proposed data fusion model has the smallest MDS scores for all sizes of the leave-out set. Moreover, the MDS scores for the stations-only model and the regression calibration approach increase as the size of the leave-out set increases. The proposed data fusion model also has the smallest RMSE, MAE, and MAPE. The prediction errors for the stations-only model and the regression calibration model increase with the size of the leave-out set. The MKLD and MSD for the proposed data fusion model is also the smallest among the three models. Figure 18 shows that the proposed data fusion model outperforms the other two approaches, and that the regression calibration approach fares better than the stations-only model.

Figure 35 in Appendix A.5 shows a comparison of LGOCV results for the relative humidity model. The results show that the proposed data fusion model outperforms the stations-only model and the regression calibration approach for all the posterior prediction scores considered. The MDS scores for the proposed data fusion model decrease even as the size of the leave-out set increases. The difference in the RMSE, MAE, and MAPE among the three approaches is relatively small for the cases when the size of the leave-out set is small, but the difference is substantially big with a large leave-out set. The MKLD and MSD of the proposed data fusion model is also substantially smaller compared to the other two models.

Finally, Figure 36 in Appendix A.5 shows a comparison of LGOCV metrics for the rainfall model. The MDS scores for the proposed data fusion model is consistently smallest for the different sizes of the leave-out set. The data fusion approach also has the smallest MAE. In terms of the RMSE and the MAPE, there is no substantial difference in the scores among the three approaches when the leave-out set is small, but for the largest leave-out set considered, the proposed data fusion model outperforms the other two methods. Lastly, the proposed data fusion model also has the smallest MSD and MKLD for all sizes of the leave-out sets considered.

The LGOCV results show that the benefits from doing data fusion for temperature and relative humidity is higher compared to that of rainfall. One potential reason for this is that the quality of the GSM outcomes for rainfall is lower compared to the other two meteorological variables which is apparent from Figure 2 and from the model results, particularly with the estimated value of $\hat{\alpha}_1 < 1$ for the rainfall data fusion model. Nonetheless,

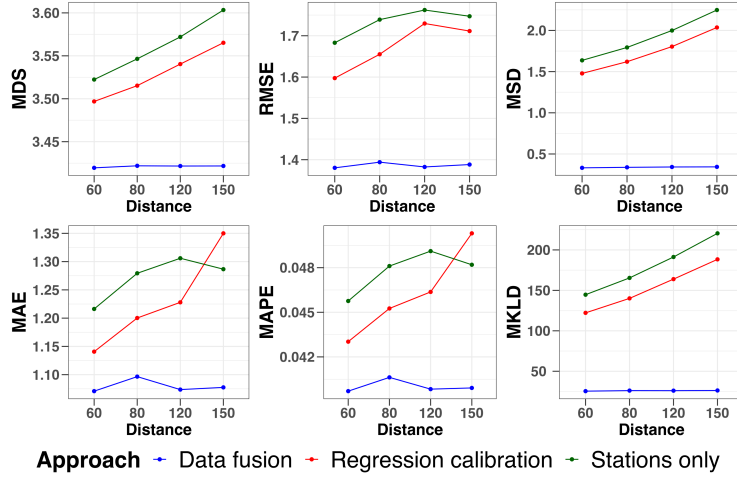


Fig. 18. Comparison of LGOCV results for temperature from three models: stations-only model, regression calibration model, and the proposed data fusion model

the LGOCV results show that the proposed data fusion model generally outperforms the other two approaches for the three meteorological variables considered.

CONCLUSIONS

Data fusion, which aims to combine information from different data sources, has the potential benefit of improving the accuracy of model estimation and the quality of model predictions while facing issues with varying qualities of the data sources [6, 21, 29]. This work addresses a data fusion problem motivated by meteorological data in the Philippines. The proposed model is based on the Bayesian melding model, which assumes a common latent process for the data sources, but we extend the model specification from related work in the literature [36, 51, 52, 18]. In particular, we specify a time-varying random field for the additive calibration bias for the outcomes from the numerical prediction model which we call an *error field*, and a constant multiplicative bias parameter. The proposed data fusion model defines a single and interpretable latent process for the data outcomes, specifies a measurement error for all data sources, gives flexibility in accounting for the different potential sources of biases, allows for several spatially-misaligned data to inform about the common latent process, and allows us to gauge the quality of the different data sources. Although we assumed that the multiplicative bias parameter α_1 is constant in this paper, the model can be extended by assuming that α_1 is spatially-varying or time-varying. This adds another layer of model complexity and also additional challenge in the computation and model estimation, but this could be more relevant for other applications.

The proposed data fusion model gave better predictions compared to the stations-only model and the regression calibration approach based on the leave-group-out cross-validation in the data application. We used the approximation of the LGOCV in INLA as proposed in [33], but we manually defined the leave-out sets in approximating the log predictive densities and in computing the posterior prediction scores. Based on the mean Dawid-Sebastiani score, the proposed data fusion model outperforms the other two approaches. The proposed data fusion model also has the smallest mean KLD between the predictive distribution from using the full data and that from excluding the leave-out sets. We also considered other posterior predictions scores such as the RMSE, MAE, MAPE, and the uncertainty (standard deviations) in the posterior predictive distributions. The proposed data fusion model generally outperforms the other two approaches, and that the discrepancy in the scores among the three approaches increases as the size of the leave-out set increases.

We conducted a simulation study in order to compare the performance of a data fusion model and a stations-only model under different levels of sparsity of the stations data and the specification of the priors of the model hyperparameters. The results of the simulation study showed that the data fusion model gave lower average squared-error of the estimated field and lower average posterior uncertainty, especially when the stations data are sparse. The data fusion model also gave lower mean Dawid-Sebastiani scores in the observational data. Lastly, the data fusion model also has smaller relative errors and smaller posterior uncertainty in the parameter estimates compared to the stations-only model.

This work considers only two data sources for meteorological data in the Philippines since these are the two primary data sources available in the country. However, the current framework can be extended to incorporate additional data sources such as satellite data. In this case, an additional likelihood model for the new observation data can be introduced, which will have its own set of bias parameters and an error field which can also be time-varying. The proposed modelling approach allows for more than two data sources, even spatially-misaligned data, to inform about the latent process of interest.

This work was primarily motivated by the meteorological data problem in the Philippines, but the proposed data fusion model is also applicable in different contexts such as in air quality modelling. As an example, in the United Kingdom, daily concentrations of air pollutants are collected by a network of monitoring stations called the Automatic Urban and Rural Network (AURN) [31]. Additional data sources for air quality are outcomes from a weather and chemistry transport model called the Air Quality Unified Model (AQUM) which is maintained by the Met Office [45], and outcomes from another dispersion model called the Pollution Climate Mapping (PCM) model which are run by Ricardo Energy & Environment [18, 16]. The proposed data fusion model in this paper allows one to model the AURN, AQUM, and PCM jointly in order to come up with good predictions of air quality, which are important for generating good forecasts of the concentration of air pollutants and for assessing the impact of these on public health and safety. As noted by [18], most of the data fusion studies for air quality modelling in the literature only consider one extra data source at a time. The proposed data fusion model in this work allows us to use the three aforementioned data sources jointly, while also allowing us to carefully account for their biases. Also, the proposed model allows us to gauge the quality of the outcomes from the numerical models by looking at the magnitude of the error field estimates and the multiplicative bias parameter. Another important area where the proposed data fusion framework is applicable is in species distributions modelling. With technological advancements, there has been a rise in data collection capabilities to study the natural world, and also an increase in the volume of data from increased participation of the general public in data collection [4, 8]. However, there is also a concern with regards to the quality of these data, referred to as *citizen science data*, due to systemic biases among others [50, 4]. The appropriate use of citizen science data together with data from well-planned surveys falls within the realm of data fusion. The proposed data fusion framework in this work views these different data sources as realized outcomes of the same latent process. The proposed data fusion model can then be extended in this context by assuming some probabilistic structure of the biases in the citizen science data while borrowing strength from the accuracy of the outcomes from well-planned surveys.

The INLA and the SPDE approach was used for model inference because they provide fast and reliable fitting of complex spatio-temporal models [41, 32]. A potential challenge in the computational aspect is that the proposed data fusion model involves a non-linear predictor, particularly the product of the multiplicative bias parameter α_1 and a Gaussian field given by $\mathbf{Z}_t \boldsymbol{\beta}_t + \boldsymbol{\xi}_t$. Although the proposed data fusion model can be estimated using a data augmentation approach [35, 42], this approach turned out to be less numerically stable. Hence, we used the model averaging approach so that we can fit the data fusion model conditional on α_1 . This is a viable approach since we have an intuitive understanding of the plausible values of this bias parameter. Another approach for fitting the model is to perform a linearization on the non-linear predictors using a first-order Taylor approximation, and to iteratively do this by looking for the optimal linearization point [47, 5]. Since the convergence of this approach and the properties of the approximation depend on the non-linear nature of the problem, it can also be computationally challenging for some cases. The use of a model averaging approach successfully removed the computational challenges due to non-linear predictors in the model, but the linearized INLA approach as previously described is also a viable approach for the problem and will be further explored in a future work.

An immediate future work is to use the predicted fields from the data fusion model as an input in an epidemiological model in order to understand the link between climate data and health outcomes. This introduces another layer of spatial misalignment since typically data for the health outcomes are areal while the predicted fields from the climate data fusion models are point-referenced. Also, in this two-stage modeling framework, accounting for the uncertainty in the data fusion model when fitting the health model should be carefully considered. The problem of uncertainty propagation has been studied in the context of health modeling [12, 31, 26] and which generally falls under the area of measurement error models [10].

COMPETING INTERESTS

We declare that there is no conflict of interest regarding the publication of this paper.

AUTHOR CONTRIBUTIONS STATEMENT

S.V.: Conceptualization, Methodology, Formal Analysis, Writing - Original Draft, Writing - Review & Editing. **J.I.:** Conceptualization, Methodology, Investigation, Writing - Review & Editing, Supervision. **S.M.:**

Conceptualization, Methodology, Investigation, Writing - Review & Editing, Supervision. **F.L.:** Methodology, Writing - Review & Editing.

ACKNOWLEDGMENTS

The authors thank the *Philippine Atmospheric, Geophysical and Astronomical Services Administration* (PAGASA) office for generously sharing the meteorological data and for providing additional model insights.

REFERENCES

1. Nur Athen Mohd Hardy Abdullah, Nazri Che Dom, Siti Aekball Salleh, Hasber Salim, and Nopadol Precha. The association between dengue case and climate: A systematic review and meta-analysis. *One Health*, page 100452, 2022.
2. A Adin, E Krainski, A Lenzi, Z Liu, J Martínez-Minaya, and H Rue. Automatic cross-validation in structured models: Is it time to leave out leave-one-out? *arXiv preprint arXiv:2311.17100*, 2023.
3. Ali Arab, Monica C Jackson, and Cezar Kongoli. Modelling the effects of weather and climate on malaria distributions in west africa. *Malaria journal*, 13:1–9, 2014.
4. Tom August, Martin Harvey, Paula Lightfoot, David Kilbey, Timos Papadopoulos, and Paul Jepson. Emerging technologies for biological recording. *Biological Journal of the Linnean Society*, 115(3):731–749, 2015.
5. Fabian E Bachl, Finn Lindgren, David L Borchers, and Janine B Illian. inlabru: an r package for bayesian spatial modelling from ecological survey data. *Methods in Ecology and Evolution*, 10(6):760–766, 2019.
6. Peter Bauer, Alan Thorpe, and Gilbert Brunet. The quiet revolution of numerical weather prediction. *Nature*, 525(7567):47–55, 2015.
7. Hylke E Beck, Niklaus E Zimmermann, Tim R McVicar, Noemi Vergopolan, Alexis Berg, and Eric F Wood. Present and future köppen-geiger climate classification maps at 1-km resolution. *Scientific data*, 5(1):1–12, 2018.
8. Jafet Belmont, Sara Martino, Janine Illian, and Håvard Rue. Spatio-temporal occupancy models with inla. *arXiv preprint arXiv:2403.10680*, 2024.
9. Veronica J Berrocal, Alan E Gelfand, and David M Holland. A spatio-temporal downscaler for output from numerical models. *Journal of agricultural, biological, and environmental statistics*, 15:176–197, 2010.
10. Scott M Berry, Raymond J Carroll, and David Ruppert. Bayesian smoothing and regression splines for measurement error problems. *Journal of the American Statistical Association*, 97(457):160–169, 2002.
11. Roger Bivand and Gianfranco Piras. Comparing implementations of estimation methods for spatial econometrics. *Journal of Statistical Software*, 63:1–36, 2015.
12. Marta Blangiardo, Francesco Finazzi, and Michela Cameletti. Two-stage bayesian model to evaluate the effect of air pollution on chronic respiratory diseases using drug prescriptions. *Spatial and spatio-temporal epidemiology*, 18:1–12, 2016.
13. Cheng Chen, Qiuwen Chen, Gang Li, Mengnan He, Jianwei Dong, Hanlu Yan, Zhiyuan Wang, and Zheng Duan. A novel multi-source data fusion method based on bayesian inference for accurate estimation of chlorophyll-a concentration over eutrophic lakes. *Environmental Modelling & Software*, 141:105057, 2021.
14. Lung-Chang Chien and Hwa-Lung Yu. Impact of meteorological factors on the spatiotemporal patterns of dengue fever incidence. *Environment international*, 73:46–56, 2014.
15. A Philip Dawid and Paola Sebastiani. Coherent dispersion criteria for optimal experimental design. *Annals of Statistics*, pages 65–81, 1999.
16. DEFRA. Uk air information resource. <https://uk-air.defra.gov.uk/research/air-quality-modelling?view=modelling>, 2024. Accessed: 2024-04-04.
17. MG Falk, RJ Denham, and KL Mengersen. Estimating uncertainty in the revised universal soil loss equation via bayesian melding. *Journal of agricultural, biological, and environmental statistics*, 15:20–37, 2010.
18. Chiara Forlani, Samir Bhatt, Michela Cameletti, Elias Krainski, and Marta Blangiardo. A joint bayesian space–time model to integrate spatially misaligned air pollution data in r-inla. *Environmetrics*, 31(8):e2644, 2020.
19. Montserrat Fuentes and Adrian E Raftery. Model evaluation and spatial interpolation by bayesian combination of observations with outputs from numerical models. *Biometrics*, 61(1):36–45, 2005.
20. Geir-Arne Fuglstad, Daniel Simpson, Finn Lindgren, and Håvard Rue. Constructing priors that penalize the complexity of gaussian random fields. *Journal of the American Statistical Association*, 114(525):445–452, 2019.
21. Andrew Gettelman, Alan J Geer, Richard M Forbes, Greg R Carmichael, Graham Feingold, Derek J Posselt, Graeme L Stephens, Susan C van den Heever, Adam C Varble, and Paquita Zuidema. The future of earth

system prediction: Advances in model-data fusion. *Science Advances*, 8(14):eabn3488, 2022.

22. Tilmann Gneiting and Adrian E Raftery. Strictly proper scoring rules, prediction, and estimation. *Journal of the American statistical Association*, 102(477):359–378, 2007.
23. Virgilio Gómez-Rubio, Roger S Bivand, and Håvard Rue. Bayesian model averaging with the integrated nested laplace approximation. *Econometrics*, 8(2):23, 2020.
24. Richard Goody. *Principles of atmospheric physics and chemistry*. 1995.
25. Sonja Greven, Francesca Dominici, and Scott Zeger. An approach to the estimation of chronic air pollution effects using spatio-temporal information. *Journal of the American Statistical Association*, 106(494):396–406, 2011.
26. Alexandros Gryparis, Christopher J Paciorek, Ariana Zeka, Joel Schwartz, and Brent A Coull. Measurement error caused by spatial misalignment in environmental epidemiology. *Biostatistics*, 10(2):258–274, 2009.
27. Darrel Hess and Dennis Tasa. *McKnight's physical geography: a landscape appreciation*. Prentice Hall Upper Saddle River, NJ, 2011.
28. I Gede Nyoman Mindra Jaya and Henk Folmer. Spatiotemporal high-resolution prediction and mapping: methodology and application to dengue disease. *Journal of geographical systems*, 24(4):527–581, 2022.
29. Andrew B Lawson, Sudipto Banerjee, Robert P Haining, and María Dolores Ugarte. *Handbook of spatial epidemiology*. CRC press, 2016.
30. A Lee, A Szpiro, SY Kim, and L Sheppard. Impact of preferential sampling on exposure prediction and health effect inference in the context of air pollution epidemiology. *Environmetrics*, 26(4):255–267, 2015.
31. Duncan Lee, Sabyasachi Mukhopadhyay, Alastair Rushworth, and Sujit K Sahu. A rigorous statistical framework for spatio-temporal pollution prediction and estimation of its long-term impact on health. *Biostatistics*, 18(2):370–385, 2017.
32. Finn Lindgren, Håvard Rue, and Johan Lindström. An explicit link between gaussian fields and gaussian markov random fields: the stochastic partial differential equation approach. *Journal of the Royal Statistical Society: Series B (Statistical Methodology)*, 73(4):423–498, 2011.
33. Zhedong Liu and Haavard Rue. Leave-group-out cross-validation for latent gaussian models. *arXiv preprint arXiv:2210.04482*, 2022.
34. Zhong Liu, Nhu D Le, and James V Zidek. An empirical assessment of bayesian melding for mapping ozone pollution. *Environmetrics*, 22(3):340–353, 2011.
35. Thiago G Martins, Daniel Simpson, Finn Lindgren, and Håvard Rue. Bayesian computing with inla: new features. *Computational Statistics & Data Analysis*, 67:68–83, 2013.
36. Paula Moraga, Susanna M Cramb, Kerrie L Mengersen, and Marcello Pagano. A geostatistical model for combined analysis of point-level and area-level data using inla and spde. *Spatial Statistics*, 21:27–41, 2017.
37. Stefanie Muff, Andrea Riebler, Leonhard Held, Håvard Rue, and Philippe Saner. Bayesian analysis of measurement error models using integrated nested laplace approximations. *Journal of the Royal Statistical Society Series C: Applied Statistics*, 64(2):231–252, 2015.
38. Suchithra Naish, Pat Dale, John S Mackenzie, John McBride, Kerrie Mengersen, and Shilu Tong. Climate change and dengue: a critical and systematic review of quantitative modelling approaches. *BMC infectious diseases*, 14(1):1–14, 2014.
39. PAGASA. Climate of the philippines. <https://www.pagasa.dost.gov.ph/information/climate-philippines>, 2023. Accessed: 2023-06-12.
40. David Poole and Adrian E Raftery. Inference for deterministic simulation models: the bayesian melding approach. *Journal of the American Statistical Association*, 95(452):1244–1255, 2000.
41. Håvard Rue, Sara Martino, and Nicolas Chopin. Approximate bayesian inference for latent gaussian models by using integrated nested laplace approximations. *Journal of the royal statistical society: Series b (statistical methodology)*, 71(2):319–392, 2009.
42. Ramiro Ruiz-Cárdenas, Elias T Krainski, and Håvard Rue. Direct fitting of dynamic models using integrated nested laplace approximations. *Computational Statistics & Data Analysis*, 56(6):1808–1828, 2012.
43. Sujit K Sahu, Alan E Gelfand, and David M Holland. Fusing point and areal level space–time data with application to wet deposition. *Journal of the Royal Statistical Society Series C: Applied Statistics*, 59(1):77–103, 2010.
44. Nathan J Sanders, Jean-Philippe Lessard, Matthew C Fitzpatrick, and Robert R Dunn. Temperature, but not productivity or geometry, predicts elevational diversity gradients in ants across spatial grains. *Global Ecology and Biogeography*, 16(5):640–649, 2007.
45. NH Savage, P Agnew, LS Davis, C Ordóñez, R Thorpe, CE Johnson, FM O'Connor, and M Dalvi. Air quality modelling using the met office unified model (aum os24-26): model description and initial evaluation. *Geoscientific Model Development*, 6(2):353–372, 2013.
46. Alexandra M Schmidt and Alan E Gelfand. A bayesian coregionalization approach for multivariate pollutant data. *Journal of Geophysical Research: Atmospheres*, 108(D24), 2003.

47. Francesco Serafini, Finn Lindgren, and Mark Naylor. Approximation of bayesian hawkes process with inlabru. *Environmetrics*, 34(5):e2798, 2023.
48. Hana Ševčíková, Adrian E Raftery, and Paul A Waddell. Uncertain benefits: Application of bayesian melding to the alaskan way viaduct in seattle. *Transportation Research Part A: Policy and Practice*, 45(6):540–553, 2011.
49. Daniel Simpson, Håvard Rue, Andrea Riebler, Thiago G Martins, and Sigrunn H Sørbye. Penalising model component complexity: A principled, practical approach to constructing priors. 2017.
50. Arco J Van Strien, Chris AM Van Swaay, and Tim Termaat. Opportunistic citizen science data of animal species produce reliable estimates of distribution trends if analysed with occupancy models. *Journal of Applied Ecology*, 50(6):1450–1458, 2013.
51. Stephen Jun Villejo, Janine B Illian, and Ben Swallow. Data fusion in a two-stage spatio-temporal model using the inla-spde approach. *Spatial Statistics*, 54:100744, 2023.
52. Ruiman Zhong and Paula Moraga. Bayesian hierarchical models for the combination of spatially misaligned data: A comparison of melding and downscaler approaches using inla and spde. *Journal of Agricultural, Biological and Environmental Statistics*, pages 1–20, 2023.

APPENDIX

Simulation Results

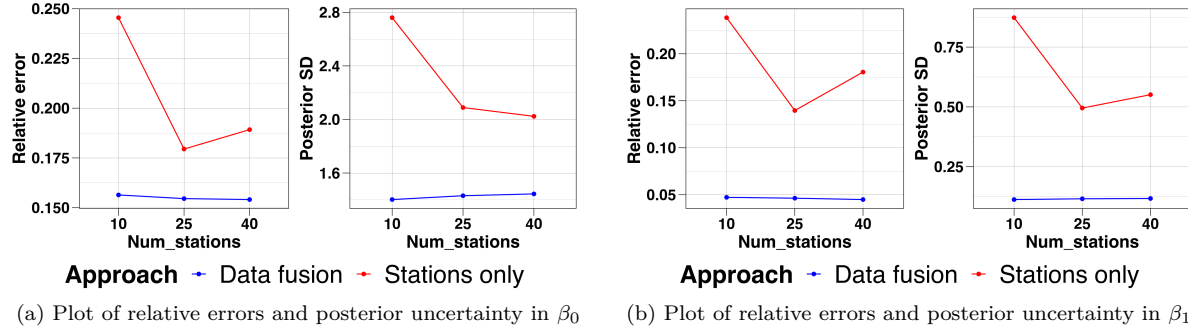


Fig. 19. Plot of average relative errors and average posterior uncertainty for the fixed effects: (a) β_0 and (b) β_1

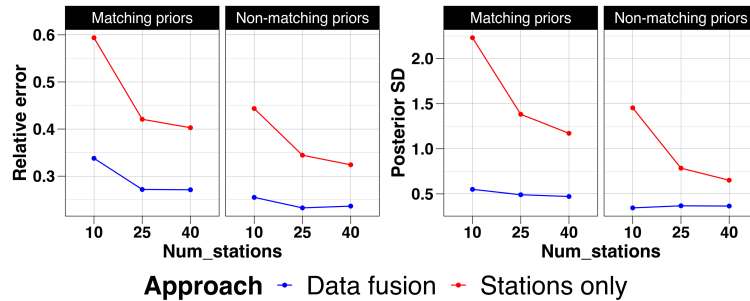


Fig. 20. Plot of average relative errors and average posterior uncertainty for ρ_ξ

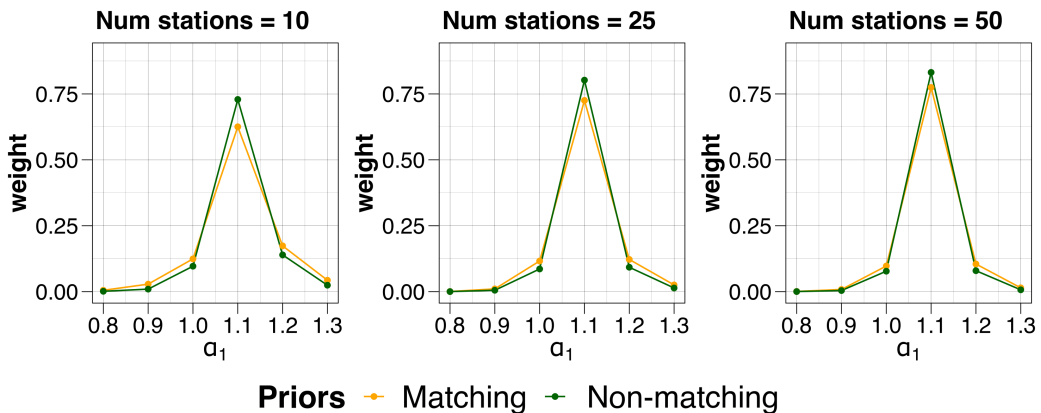


Fig. 21. Average model averaging weights for different α_1 values in fitting the proposed data fusion model with respect to the sparsity of the stations data and the priors used. The correct value of α_1 has the highest weight.

Temperature model

Table 4. Marginal log-likelihoods conditional an α_1 and the corresponding BMA weights for the temperature data fusion model

α_1	$\log \pi(\mathbf{Y} \alpha_1)$	w_k
0.5	-978.2951	0.0000
0.6	-914.7904	0.0000
0.7	-849.6732	0.0000
0.8	-778.4929	0.0000
0.9	-697.5013	0.0001
1	-688.1419	1.0000
1.1	-811.9266	0.0000
1.2	-899.7620	0.0000
1.3	-949.7187	0.0000
1.4	-2265.0736	0.0000
1.5	-2329.8480	0.0000

Table 5. Posterior estimates of hyperparameters for the temperature model - stations-only model versus proposed data fusion model

Parameter	Stations only				Data fusion			
	Mean	SD	P2.5%	P97.5%	Mean	SD	P2.5%	P97.5%
σ_{e_1}	0.1781	0.0106	0.1581	0.1967	0.2429	0.0103	0.2241	0.2636
σ_{e_2}	-	-	-	-	0.0221	0.0068	0.0145	0.0430
ρ_1	621.8876	50.6769	528.7427	728.1444	764.7483	59.3223	655.5974	888.9635
σ_1	5.1208	0.6116	4.0336	6.4384	7.6904	0.8720	6.1331	9.5545
ϕ_1	0.9920	0.0023	0.9879	0.9951	0.9979	0.0005	0.9968	0.9987
ρ_2	-	-	-	-	112.7677	8.0757	97.7734	129.5544
σ_2	-	-	-	-	0.6681	0.0662	0.5465	0.8065
ϕ_2	-	-	-	-	0.9371	0.0137	0.9060	0.9596

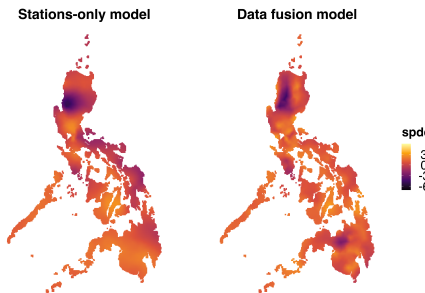


Fig. 22. Comparison of estimated spatial fields $\xi(s, t)$ for August 2019 between the stations-only model versus proposed data fusion model. The estimated spatial fields are roughly similar.

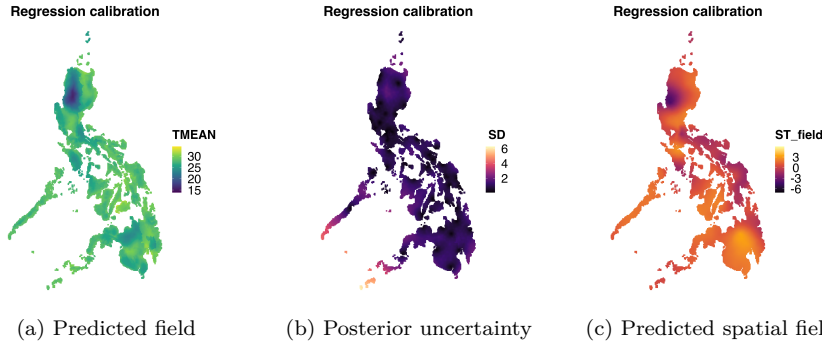


Fig. 23. Model results from the regression calibration approach for temperature: (a) estimated temperature field (b) posterior standard deviation (c) estimated spatial field

Table 6. Posterior estimates for the temperature model - regression calibration approach

Parameter	Mean	SD	P2.5	P97.5
β_0	6.7283	5.7536	-4.5485	18.0051
$\beta_1, \log(\text{Elevation})$	-0.4324	0.0958	-0.6202	-0.2447
β_2, Cool	-0.6835	0.1994	-1.0743	-0.2927
$\beta_3, \text{Climate Type}$	2.1489	0.6177	0.9382	3.3595
β_4, GSM	0.8293	0.1982	0.4409	1.2178
σ_{e_1}	0.1824	0.01078	0.1616	0.2017
ρ_1	625.5146	51.2126	531.2444	732.7520
σ_1	4.5273	0.5445	3.5349	5.6755
ρ_1	0.9898	0.0024	0.9842	0.9936

Relative humidity model

Table 7. Marginal log-likelihoods conditional an α_1 and the corresponding BMA weights for the relative humidity data fusion model

α_1	$\log \pi(\mathbf{Y} \alpha_1)$	w_k
0.5	5955.3408	0.0000
0.6	5830.2520	0.0000
0.7	6076.5968	0.0000
0.8	6136.2539	0.0000
0.9	5320.3512	0.0000
1	6248.2818	1
1.1	6116.9061	0.0000
1.2	6101.2002	0.0000
1.3	6071.8142	0.0000
1.4	6044.1221	0.0000
1.5	5847.2576	0.0000

Table 8. Posterior estimates of hyperparameters for the relative humidity model - stations-only model versus proposed data fusion model

Parameter	Stations only				Data fusion			
	Mean	SD	P2.5%	P97.5%	Mean	SD	P2.5%	P97.5%
σ_{e_1}	0.0123	0.0008	0.0109	0.0137	0.0199	0.0010	0.0181	0.0218
σ_{e_2}	-	-	-	-	0.0029	0.0008	0.0016	0.0045
ρ_1	287.5769	26.9517	238.1271	344.1479	589.1127	67.9761	468.3741	735.5712
σ_1	0.0872	0.0078	0.0729	0.1034	0.1112	0.0141	0.0866	0.1419
ϕ_1	0.9282	0.0121	0.9018	0.9491	0.9700	0.0079	0.9522	0.9829
ρ_2	-	-	-	-	117.2557	8.9556	100.4029	135.6345
σ_2	-	-	-	-	0.0404	0.0020	0.0366	0.0446
ϕ_2	-	-	-	-	0.8553	0.0152	0.8235	0.8834

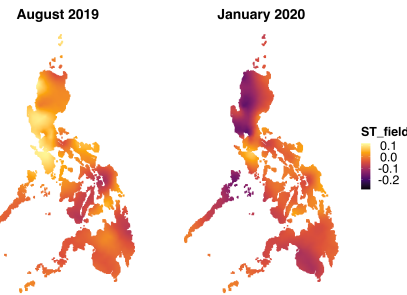


Fig. 24. Estimated spatial fields for log relative humidity, August 2019 and January 2020, using the stations-only model

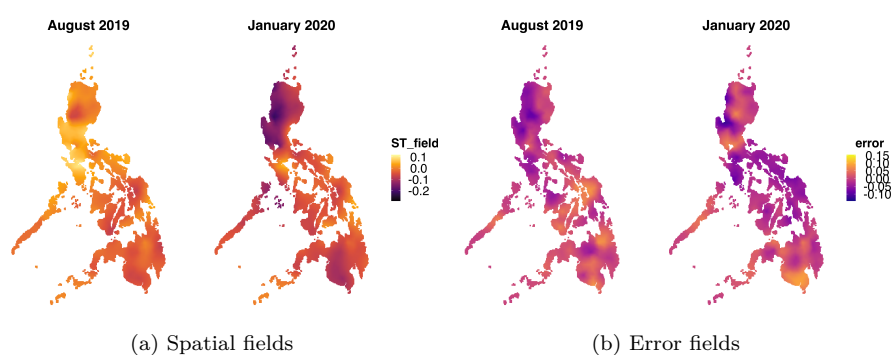


Fig. 25. Estimated spatial fields for log relative humidity (left) and estimated error fields for the GSM log relative humidity data (right), August 2019 and January 2020, using the proposed data fusion model

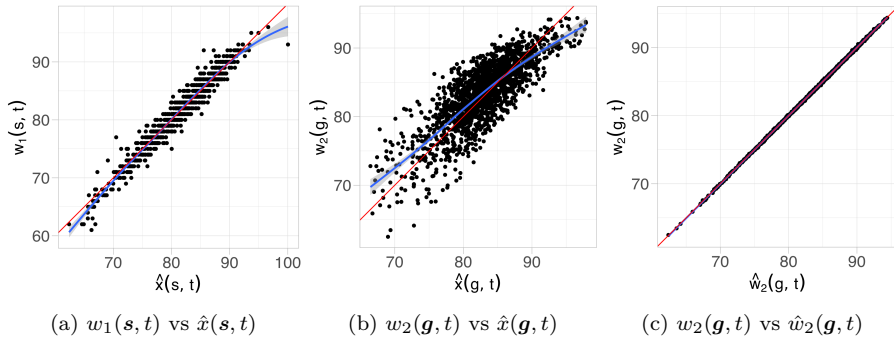


Fig. 26. Plot of observed relative humidity values versus predicted values using the proposed data fusion model for (a) weather stations and (b) GSM data, and (c) calibrated GSM data

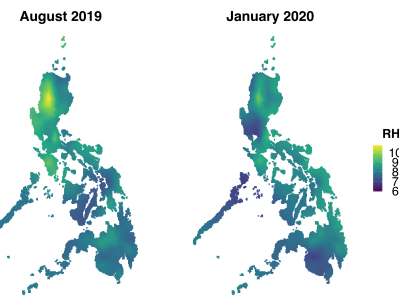


Fig. 27. Estimated relative humidity fields for August 2019 and January 2020 using the regression calibration approach

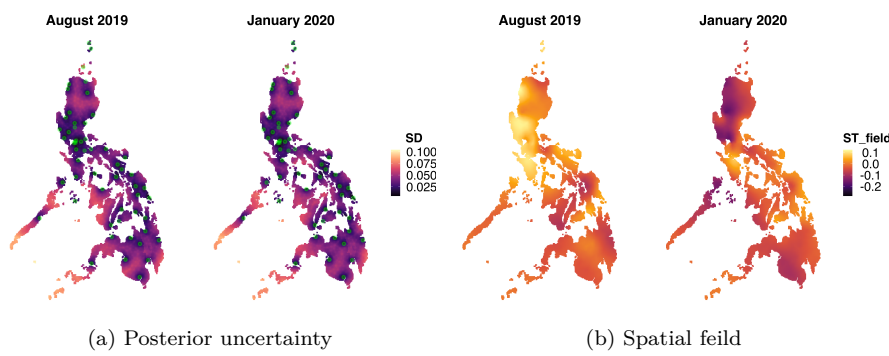


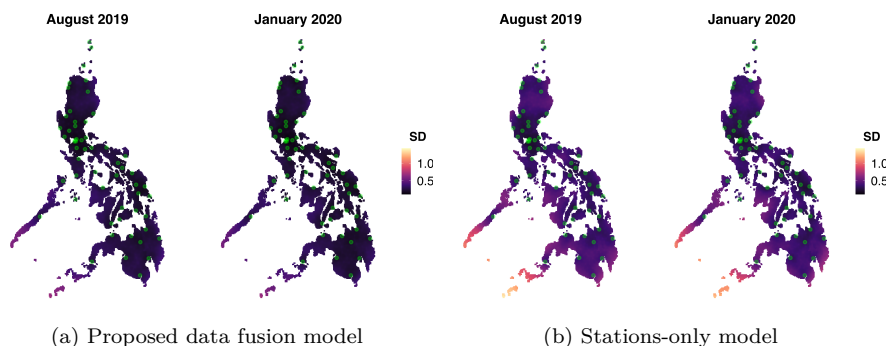
Fig. 28. Estimated posterior uncertainty for log relative humidity field (left) and estimated spatial field for relative humidity (right), August 2019 and January 2020, using the regression calibration approach

Table 9. Posterior estimates for the relative humidity model - regression calibration approach

Parameter	Mean	SD	P2.5	P97.5
β_0	3.7515	1.2240	1.3526	6.1505
$\beta_1, \log(\text{Temp})$	0.5608	0.0490	0.4647	0.6568
$\beta_2, \log(\text{Temp})^2$	-0.1714	0.0147	-0.2002	-0.1425
$\beta_3, \log(\text{Elevation})$	-0.0083	0.0030	-0.0142	-0.0024
$\beta_4, \text{Climate Type}$	0.0252	0.0187	-0.0116	0.0619
β_5, GSM	0.1585	0.2775	-0.3853	0.7023
σ_{e_1}	0.0124	0.001	0.0108	0.0139
ρ_1	288.0160	26.9687	238.8441	344.9359
σ_1	0.0874	0.0078	0.0731	0.1039
ρ_1	0.9287	0.0120	0.9024	0.9497

Rainfall**Table 10.** Posterior estimates of hyperparameters for the rainfall model - stations-only model versus proposed data fusion model

Parameter	Stations only				Data fusion			
	Mean	SD	P2.5%	P97.5%	Mean	SD	P2.5%	P97.5%
σ_{e_1}	0.4817	0.0193	0.4459	0.5208	0.5006	0.0218	0.4662	0.5493
σ_{e_2}	-	-	-	-	0.2560	0.0139	0.2290	0.2840
ρ_1	614.6165	62.4983	501.6406	747.4644	584.2587	59.8174	480.0420	711.3533
σ_1	1.1130	0.0737	0.9759	1.2658	1.1066	0.0650	0.9780	1.2265
ϕ_1	0.6014	0.0484	0.5014	0.6917	0.6913	0.0369	0.6107	0.7542
ρ_2					434.9348	66.3488	323.0664	588.1861
σ_2	-	-	-	-	0.9418	0.0953	0.7638	1.1157
ϕ_2	-	-	-	-	0.8696	0.0225	0.8201	0.9081

**Fig. 29.** Posterior uncertainty of the estimated log rainfall fields in Figure 16. The posterior uncertainty in the estimated fields from using the stations-only model is higher.

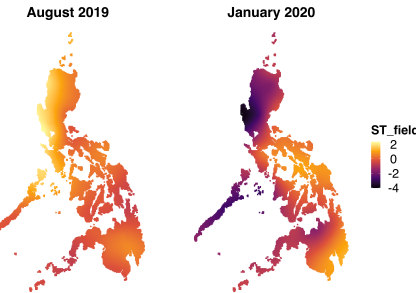


Fig. 30. Estimated spatial fields for log rainfall, August 2019 and January 2020, using the stations-only model

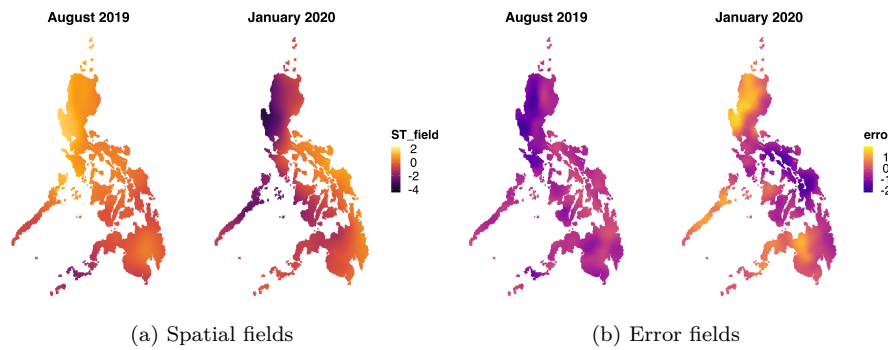


Fig. 31. Estimated spatial fields for log rainfall (left) and estimated error fields for the GSM log rainfall data (right), August 2019 and January 2020, using the proposed data fusion model

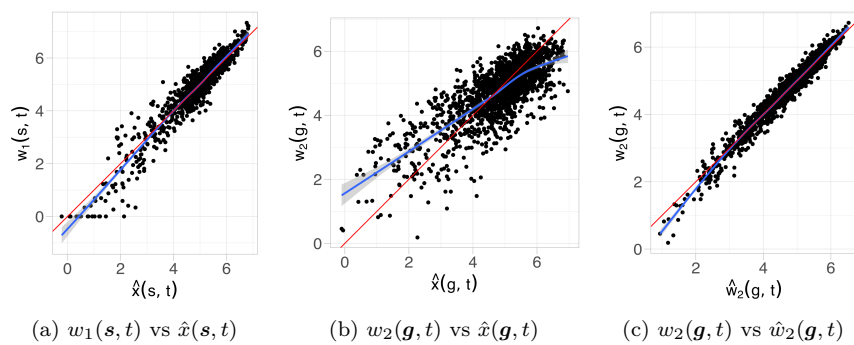


Fig. 32. Plot of observed log rainfall values versus predicted values using the proposed data fusion model: (a) weather stations, (b) GSM data, (c) calibrated GSM data

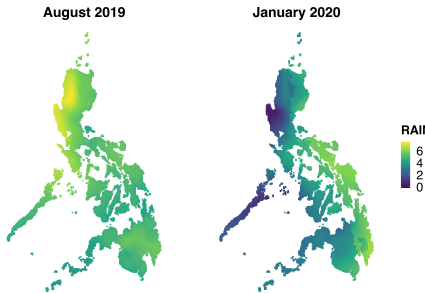


Fig. 33. Estimated log rainfall fields for August 2019 and January 2020 using the regression calibration approach

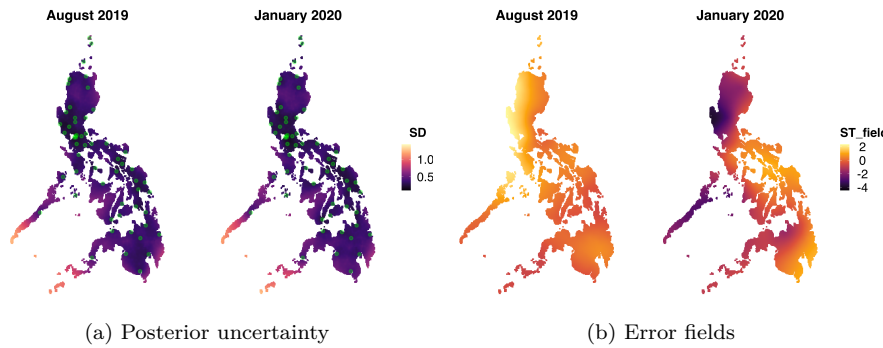


Fig. 34. Estimated posterior uncertainty for log rainfall field (left) and estimated spatial fields for log rainfall (right), August 2019 and January 2020, using the regression calibration approach

Table 11. Posterior estimates for the rainfall model - regression calibration approach

Parameter	Mean	SD	P2.5	P97.5
β_0	6.2004	1.0181	4.2051	8.1958
β_1 , log(Temp)	1.5734	0.5533	0.4891	2.6578
β_2 , log(Temp) ²	-0.5133	0.1647	-0.8361	-0.1905
β_3 , Season	0.8063	0.3074	0.2038	1.4088
β_4 , Climate Type	1.1589	0.1448	0.8752	1.4426
β_5 , Climate Type \times Season	-0.8526	0.1612	-1.1685	-0.5367
β_6	-0.0687	0.0367	-0.1407	0.0033
σ_{e_1}	4.3337	0.3722	3.6447	5.1091
ρ_1	619.7900	63.1403	506.0104	754.3626
σ_1	1.1030	0.0727	0.9678	1.2539
ρ_1	0.5909	0.0494	0.4887	0.6829

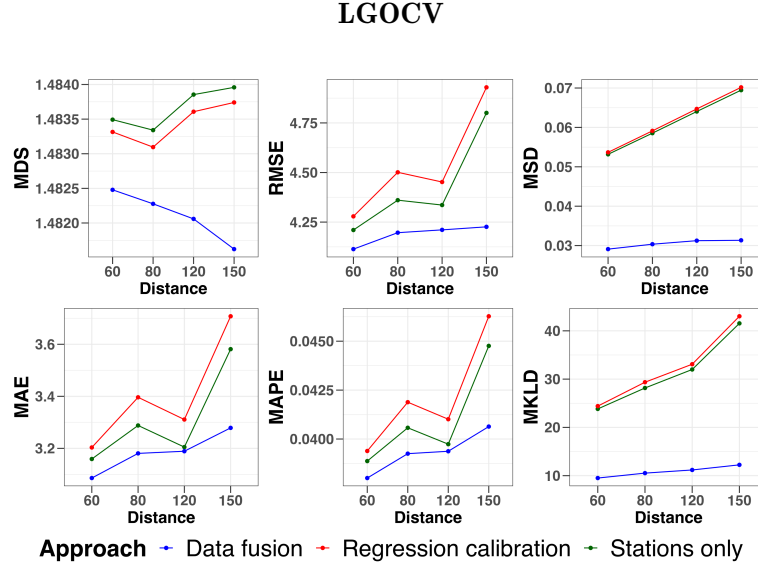


Fig. 35. Comparison of LGOCV results for relative humidity from three models: stations-only model, regression calibration model, and the proposed data fusion model

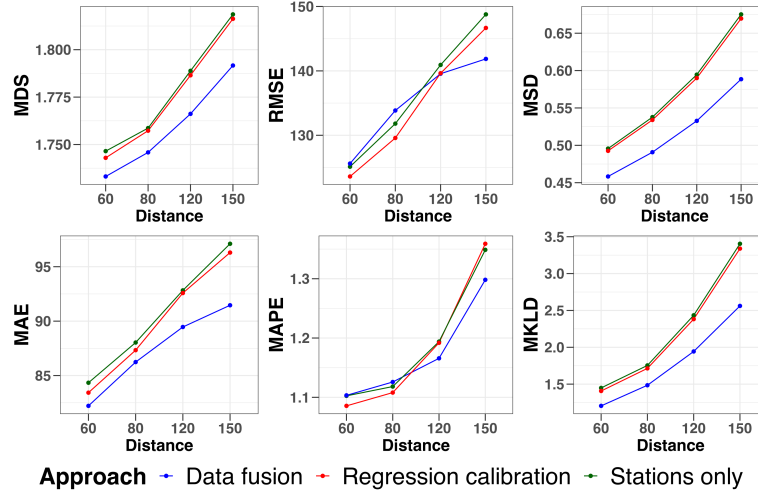


Fig. 36. Comparison of LGOCV results for rainfall from three models: stations-only model, regression calibration model, and the proposed data fusion model